

SN 1993J VLBI (III): THE EVOLUTION OF THE RADIO SHELL

M. F. BIETENHOLZ¹, N. BARTEL¹, AND M. P. RUPEN²
Draft version November 4, 2018

ABSTRACT

A sequence of images of supernova 1993J at 30 epochs, from 50 d to ~ 9 yr after shock breakout, shows the evolution of the expanding radio shell of an exploded star in detail. The images were obtained from 24 observing sessions at 8.4 GHz and 19 at 5.0 GHz and from our last session at 1.7 GHz. The images are all phase-referenced to the stable reference point of the core of the host galaxy M81. This allows us to display them relative to the supernova explosion center. The earliest image shows an almost unresolved source with a radius of 520 AU. The shell structure becomes discernible 175 d after shock breakout. The brightness of the ridge of the projected shell is not uniform, but rather varies by a factor of two, having a distinct peak or maximum to the south-east and a gap or minimum to the west. Over the next ~ 350 d, this pattern rotates counter-clockwise, with the gap rotating from west to north-northeast. After two years, the structure becomes more complex with hot spots developing in the east, south, and west. The pattern of modulation continues to change, and after five years the hot spots are located to the north-northwest, south and south-southeast. After nine years, the radio shell has expanded to a radius of 19,000 AU. The brightness in the center of the images is lower than expected for an optically thin, spherical shell. Absorption in the center is favored over a thinner shell in the back and/or front. Allowing for absorption, we find the thickness of the shell is $25 \pm 3\%$ of its outer radius. We place a 3σ upper limit of 4.4% on the mean polarization of the bright part of the shell, consistent with internal Faraday depolarization. We find no compact source in the central region above a brightness limit of $0.05 \text{ mJy beam}^{-1}$ at 8.4 GHz, corresponding to 30% of the current spectral luminosity of the Crab Nebula. We conclude that either any pulsar nebula in the center of SN 1993J is much fainter than the Crab or that there is still significant internal radio absorption.

Subject headings: supernovae: individual (SN 1993J) — radio continuum: supernovae

1. INTRODUCTION

SN 1993J is one of the brightest radio supernovae ever detected (e.g., Weiler et al. 2002). Its location in the nearby spiral galaxy M81 high in the northern sky has made it the best target for VLBI supernova studies so far. This paper is the third in a series presenting the results from our VLBI campaign on this supernova (Bietenholz, Bartel & Rupen, 2001, Paper I; Bartel et al. 2002, Paper II), and for the convenience of the reader we repeat the following two introductory paragraphs from Paper II below.

SN 1993J was discovered in a spiral arm of M81 south south-west of the galaxy's center by Garcia (Ripero & Garcia 1993) on 28 March 1993 shortly after shock breakout at ~ 0 UT ($t = 0$) on the same day (Wheeler et al. 1993). It subsequently became the optically brightest supernova in the northern hemisphere since SN 1954A. At a Cepheid-distance of 3.63 ± 0.31 Mpc (Ferrarese et al. 2000; see also Freedman et al. 1994, 2001), it is also one of the closest extragalactic supernovae ever observed and is second only to SN 1987A as a subject of intense observational and theoretical supernova studies. The precursor was identified soon after the supernova discovery (e.g., Humphreys et al. 1993) and found to be an approximately K0 I supergiant with a likely mass of $\sim 17 M_{\odot}$ (Aldering, Humphreys, & Richmond 1994; Van Dyk et al. 2002) and a radius $\geq 675 R_{\odot}$ or ≥ 3.5 AU (Clocchiatti et al. 1995).

The light curve and the spectral properties indicated that SN 1993J was of Type IIb, characterized by a low-

mass hydrogen outer layer. Höflich, Langer, & Duschinger (1993) considered a massive ($\sim 30 M_{\odot}$) single supergiant that had lost most of its hydrogen envelope through a strong wind and retained an envelope mass of $\sim 3 M_{\odot}$ (but see also Höflich 1995). However it is more likely that the progenitor had the lower mass given above, and a close binary companion that stripped off most of its hydrogen envelope. The progenitor was then left with a residual hydrogen mass in the outer shell probably in the range of 0.2 to $0.4 M_{\odot}$ (e.g., Podsiadlowski et al. 1993; Woosley et al. 1994; Houck & Fransson 1996) with some estimates being larger, but none greater than $0.9 M_{\odot}$ (Nomoto et al. 1993; Shigeyama et al. 1994; Bartunov et al. 1994).

The ejecta thrown off in the supernova explosion expand into, and interact with, the circumstellar medium (CSM), which is expected to consist of the slow, dense wind of the progenitor. In the period before the star died, the progenitor is thought to have had lost mass with a mass-loss to wind-velocity ratio $\dot{M}/w = 5 \times 10^{-5} M_{\odot}/10 \text{ km s}^{-1}$ (Van Dyk et al. 1994; Fransson & Björnsson 1998). As the ejecta expand into the CSM, it is expected that a forward shock is driven into the surrounding CSM, and a reverse shock driven back into the expanding ejecta. The radio emission is synchrotron emission, which is most likely generated by relativistic particles accelerated in the region between these two shocks (e.g., Chevalier 1982a).

In the case of SN 1993J, there may have been asymmetries in the ejecta and anisotropic expansion velocities. In particular, asymmetric spectral lines were ob-

¹ Department of Physics and Astronomy, York University, Toronto, M3J 1P3, Ontario, Canada

² National Radio Astronomy Observatory, Socorro, New Mexico 87801, USA

served (e.g., Lewis et al. 1994; Spyromilio 1994), and significant time-variable optical polarization was found in the spectra (Trammell, Hines, & Wheeler 1993; Tran et al. 1997). While the asymmetry in at least one line was possibly caused by line blending (Houck & Fransson 1996), the detection of the polarization is a strong argument for asymmetry in the optical emission region and led to ejecta models with non-spherical geometries (e.g., Höflich 1995; Höflich et al. 1996).

There are a number of different mechanisms which might produce asymmetry in the ejecta of a supernova. Some of them operate even before the shock breaks out through the surface of the progenitor. For instance, an axisymmetric density distribution of the progenitor might lead to an asymmetric explosion and an anisotropic expansion pattern. Also, recent numerical modeling of massive star explosions suggests that shortly after the bounce, the expansion has fundamentally anisotropic components and develops “fingers” with speeds twice the average expansion speed. If the CSM is anisotropic, as is expected of some red giant winds, further anisotropy could develop after shock breakout. Finally, the contact surface between the ejecta and the CSM is subject to the Rayleigh-Taylor instability, which, with time, could lead to fingers of shocked envelope material extending into the shocked CSM. A detailed sequence of images of the radio structure of the supernova is therefore of particular importance because it may allow us to see some of these mechanisms in action.

Early VLBI observations of SN 1993J allowed the size of the partly resolved supernova to be determined (Bartel et al. 1993, 1994; Marcaide et al. 1993, 1994). The radio source was shown to be circular within 5% (Bartel et al. 1994). As the supernova expanded further, a shell morphology could be discerned (Marcaide et al. 1995a, b; Bartel, Bietenholz, & Rupen 1995). More accurate measurements over seven years of observations allowed us to show that the radio shell’s 20% contour was circularly symmetric even within 3%, and that its angular expansion from the explosion center isotropic within 5.5% (Paper I). The observed highly isotropic expansion from the explosion center is in stark contrast to the anisotropic expansion suggested by the optical observations. In this context, a detailed investigation of the structure of the radio shell and its evolution with time becomes of particular importance.

The first angular expansion velocity determinations, when compared with optical velocity measurements, showed that the radio emission emanates from the shock region (Bartel et al. 1994). Subsequently, the expansion of the supernova underwent several changes. At 30 days after shock breakout ($t = 30$ d), the shell was expanding at $\sim 17,200$ km s $^{-1}$. From then till $t \sim 300$ d, the shell was slightly decelerated, with the outer radius, $\theta_o \propto t^m$ and $m = 0.919 \pm 0.019$. Then the deceleration grew significantly till $t \sim 1600$ d, with m decreasing to ~ 0.74 and the expansion velocity slowing to ~ 8900 km s $^{-1}$. Subsequently, the deceleration lessened again, with m increasing to ~ 0.85 . These changes were related to changes of the radio light-curves and the spectra, and interpreted in terms of a stratification of the ejecta, with the high-mass ejecta starting to pass through the reverse shock and ex-

erting greater pressure on the shocked low-mass envelope and the shocked CSM (Paper II; see also Mioduszewski, Dwarkadas, & Ball 2001).

In Paper I, we located the explosion center with respect to the core of the core-jet source M81*, thus defining a stable reference point for our images. We also determined, using model-fitting, an upper limit to the proper motion of the geometric center of SN 1993J, and consequently on anisotropic expansion of the radio shell. In Paper II, we determined the expansion speed of SN 1993J, measured its deceleration, and studied the radio light curves and the related changes in the radio spectrum. In this third paper, we present a complete series of VLBI images of SN 1993J at 8.4 and 5.0 GHz, along with our latest image at 1.7 GHz. While some of these images have already been presented earlier (see Papers I, II; Bietenholz et al. 2001; Bartel et al. 2000; Bartel, Bietenholz, & Rupen 1995), we present here a complete and uniform set of images from 50 d after shock breakout till the present. These images form the most complete set of images of an expanding supernova ever obtained. (For some parallel observations with up to seven consecutive images, see Marcaide et al. 1995b, 1997, 2002).

2. OBSERVATIONS AND DATA REDUCTION

From 1993 to 2001 we made 66 multi-frequency VLBI observations at 34 epochs at 22.2, 15.0, 8.4, 5.0, 2.3, and 1.7 GHz. We used a global array of between 11 and 18 telescopes with a total time of 12 to 18 hours for each epoch. These observations were described in Papers I and II. At 22.2 and 15.0 GHz, the supernova was only bright enough for useful observations in the first year. Even at the higher resolution available in principle at these frequencies, only the size but not yet the structure of the source could be determined. In particular, the gain in angular resolution at 15 GHz over that at 8.4 GHz with a comparable array was offset by the unavailability of European VLBI Network (EVN) or Deep Space Network (DSN) antennas at the higher frequency. In consequence, even during the first year, we obtained the best data for imaging at 8.4 GHz.

The high declination of 69° of SN 1993J enabled us to obtain essentially 100% visibility at almost every telescope, and as a result dense, fairly uniform, and nearly circular u - v coverage for many of our observations. In Figure 1 we show as an example the u - v coverage for the 8.4 GHz observations on 2000 November 13 ($t = 2787$ d). Most of the observations were made by phase-referencing to M81* (Bietenholz, Bartel, & Rupen, 2000), providing a combination of unsurpassed sensitivity for imaging and accurate astrometry for tracking the position of the explosion center in the images for essentially all epochs.

We used a global array of between 9 and 18 telescopes with a total time of 9 to 18 hours for each run³. The data were recorded with either the MK III or the VLBA/MKIV VLBI systems, and correlated with the NRAO VLBA processor in Socorro, New Mexico, USA. The analysis was carried out using NRAO’s Astronomical Image Processing System (AIPS). The usual procedure in calibrating VLBI data is to determine the instrumental phases, which are

³ see Paper II for further details of the arrays used at each session except for the 5 GHz epoch at 2002 May 25, for which the details are identical to that of 1999 June 16, with the exception that Nt did not observe, and that the total time was 11.8 hours and the on-source time was 439 baseline-hours.

essentially unknown, by self-calibration using an arbitrary starting model which is typically a point source (Walker 1999). While this procedure generally converges well, it can introduce symmetrizing artifacts into the images (Lindfield 1986; Massi & Aaron 1999). Phase-referencing allowed us to calibrate the instrumental phases with respect to M81* to the extent that we no longer needed to self-calibrate with an arbitrary starting model, and thus avoided any symmetrization. We are thus assured of the most un-biased images possible. In those cases where the signal-to-noise ratio was sufficiently high we proceeded to self-calibrate in phase, using the phase-referenced image as a model, to further improve the images. In fact, for later epochs phase-referencing was necessary for any imaging of SN 1993J, since the decreasing flux density made self-calibration impossible.

All the images were deconvolved with the CLEAN algorithm, using the robust weighting scheme implemented in the AIPS task IMAGR (Briggs 1995; Briggs, Schwab, & Sramek 1998). For imaging, the (calibrated) complex correlation coefficients are usually weighted by the inverse of the thermal noise variance. Since residual calibration errors may be present in the data and need not scale with the thermal noise, we compressed the weights somewhat by weighting with the inverse of the rms, rather than the usual variance, of the thermal noise.

Despite the mostly superb u - v coverage, differences from epoch to epoch in the number of antennas and their scheduled time for the observations caused variations in the effective angular resolution at each frequency. In particular, the parameters of an elliptical Gaussian fit to the inner portion of the “dirty beam” varied from epoch to epoch. We aimed for the most consistent representation of the images in each sequence to facilitate inter-comparison of the images, and to minimize any possible misinterpretation due to a varying angular resolution. For this purpose, we present the sequences of images at 8.4 and at 5.0 GHz each convolved with circular Gaussian restoring beams whose widths increase monotonically with time. Since the resolution is naturally somewhat lower at 5.0 GHz than at 8.4 GHz, a somewhat larger beam was used at 5.0 GHz in the early images. In the later images, the increased dynamic range at 5 GHz compared to that at 8.4 GHz allowed us to use the same restoring beam at both frequencies, which allows for better comparison of the images at the two frequencies. In general, we chose the width of the convolving beam to be approximately equal to, or somewhat larger than, the maximum axis of the elliptical Gaussian fit to the inner portion of the “dirty beam.” In a few early cases, we mildly super-resolved our images along one or both axes of the dirty beam, and these cases are noted in

Table 1. In the later images, because of the low signal-to-noise ratio, we choose a restoring beam somewhat larger than the inner portion of the dirty beam. In the remainder of this paper, when we refer to the resolution of an image, we mean the full width at half maximum (FWHM) of the Gaussian convolving beam⁴.

3. THE SEQUENCES OF IMAGES

In Figure 2 we display 24 images of the supernova at 8.4 GHz along with 19 images at 5.0 GHz. In addition, we display the 8.4 GHz images in false color in Figure 3. In Table 1 we give key characteristics of each of these images. In Figure 4 we show our most recent image, observed at 1.7 GHz on 2001 November 26 ($t = 3164$ d). In each image, we take the geometric center of the supernova shell as the origin of the coordinate system. In particular, we describe in Paper I how we fit a geometric spherical shell model⁵ directly to the u - v data. It is the center of this fit model we take as the geometric center of the shell.

In Paper I, we determined the coordinates of the explosion center. At 8.4 GHz, the positions of the geometric center at each epoch are tabulated as offsets from the coordinates of the center of explosion, $\alpha_{\text{explosion}} = 09^{\text{h}} 55^{\text{m}} 24.^{\text{s}}7747593$, $\delta_{\text{explosion}} = 69^{\circ} 01' 13''.703188$ (J2000), for all but the last two epochs for which the data reduction was not complete at the time that Paper I was published. The rms variation of these offsets is $64 \mu\text{as}$, and is not significantly different from the combined standard errors of the shell center and explosion center positions of $60 \mu\text{as}$.

The images show the dynamic evolution of the expanding radio shell from 50 d to 3345 d after the explosion. Never before has it been possible to obtain such detailed information on the radio emission from a supernova. With phase-referencing, dense u - v coverage, and the use of essentially the most sensitive array available for such observations, the images are of the highest quality that could be obtained for the time of the observations. The most sensitive observations were those of our last epoch at 5.0 GHz. The standard deviation of the background brightness was just $16 \mu\text{Jy beam}^{-1}$ and the peak brightness in the image was $420 \mu\text{Jy beam}^{-1}$ (see Table 1), giving us a nominal dynamic range of 26, among the highest ever obtained for such a weak source.

In Figure 5 we plot the mean spectral volume emissivity, ϵ_v , and brightness temperature, T_b , for SN 1993J for each of the images in Fig. 2. We calculate ϵ_v and T_b from the total flux densities and fit outer radii, θ_o , from Paper II. For ϵ_v we take a distance of 3.6 Mpc and assume a spherical shell with ratio of the outer to the inner radius of 1.34. At 8.4 GHz, ϵ_v declines from a

⁴ The exact procedure we used to make our final images was as follows: We first adjusted the weighting scheme via the Briggs’ robustness parameter to achieve a dirty beam with FWHM close to but somewhat smaller than the desired resolution. We then followed the usual procedure in making a restored CLEAN image of convolving the CLEAN components with the elliptical Gaussian “CLEAN beam” fitted to the inner portion of the dirty beam, and then adding the (un-deconvolved) residuals from the CLEAN deconvolution. We finally re-convolved the whole restored image, now including the residuals, to the desired effective circular Gaussian resolution. This procedure serves to keep the residuals at approximately the same effective resolution as the CLEAN components. However, the CLEANing process was carried on well into the noise in all cases, so any contribution from un-CLEANed residuals over the extent of SN 1993J was minimal.

⁵ The model consisted of the two-dimensional projection of a three-dimensional spherical shell with uniform volume emissivity and with the ratio of the outer to inner angular radius, $\theta_o/\theta_i = 1.25$ corresponding to a shell thickness, $\theta_o - \theta_i$, of $0.2\theta_o$ (see Paper I for details). The use of a circular model despite the evident modulation of the shell brightness is justified because, as we show in Paper I, SN 1993J remains circular to within 3%. Furthermore, as we show in Paper II, the fit size of the spherical shell evolves very smoothly, which suggests that, despite the modulation of the brightness around the ridge of the projected shell, the uniform spherical shell model is a good overall description of SN 1993J’s radio emission.

value of $(1.1 \pm 2) \times 10^{-22} \text{ erg cm}^{-3} \text{ Hz}^{-1} \text{ s}^{-1}$ at $t = 50 \text{ d}$ to $(4.9 \pm 0.5) \times 10^{-27} \text{ erg cm}^{-3} \text{ Hz}^{-1} \text{ s}^{-1}$ at $t = 2787 \text{ d}$. The behavior at 5.0 GHz is very similar, but the values are $\sim 40\%$ higher. The behavior of T_b is very similar to that of ϵ_v , and at 8.4 GHz T_b declines from a value of $(2.3 \pm 0.3) \times 10^{10} \text{ K}$ at $t = 50 \text{ d}$ to $(3.3 \pm 0.2) \times 10^6 \text{ K}$ at $t = 2787 \text{ d}$. The peak brightness temperatures, assuming features the size of the beam, are higher than the average values by a factor of ~ 2 for the epochs at which SN 1993J was clearly resolved.

3.1. General Aspects of the Changing Brightness Distribution

Before we focus on the individual images and specific features therein, we study the general aspects of the evolving brightness distribution of the expanding radio shell. At early epochs, with $t < 175 \text{ d}$, SN 1993J is still unresolved. The shell structure first becomes visible at $t = 175 \text{ d}$, and it remains so for all our subsequent images. As we have already shown in Papers I and II, the shell remains remarkably circular in projection. Perhaps the most striking overall feature of the structure is that the brightness of the projected shell is quite strongly modulated in position angle, p.a., despite the circularity of the outer contours. In fact, even at the earliest epoch where the shell is resolved ($t = 175 \text{ d}$) the brightness around the ridge varies by a factor of ~ 2 , with a pronounced maximum or peak at p.a. $\sim 135^\circ$ and a minimum or gap at p.a. $\sim -90^\circ$. At late times, the modulation has become more complex, and there is no longer such a clear one-sided pattern. To illustrate this behavior more clearly, we show in Figure 6 the 8.4 GHz images at $t = 264$ and 2525 d , both convolved to the same relative resolution of $0.73\times$ the shell outer angular radius as determined in Paper II. The shell appears much more uniform at $t = 2525 \text{ d}$.

We defer detailed discussion of the reliability of the images and the uncertainties to the following sections, but we make some general remarks here. A strong argument for the reality of the observed modulation of the shell brightness is the excellent correspondence between the images at 8.4 and 5.0 GHz which is clearly visible in Figure 2. The slow changes from epoch to epoch visible also in Figure 2 further argue for the reality of the structure observed.

In order to discuss the modulation of the brightness around the ridge, we introduce the following simple parameterization. For simplicity, we consider only modulation of the two-dimensional brightness distribution with p.a. Let l be the wave number of a sinusoidal modulation with p.a. of the projected shell, such that there are l maxima around the circumference. We plot the amplitude and phase of the first three sinusoids with $l = 1, 2, 3$ at 8.4 GHz, at which frequency the resolution is higher for early epochs, in Figure 7.

At $t = 264 \text{ d}$ the amplitude of the $l = 1$ modulation is quite large, and increases further till $t = 306 \text{ d}$. It is possible that this early rise is a resolution effect, since a finite resolution will tend to suppress the apparent modulation. After $t = 306 \text{ d}$, the $l = 1$ amplitude falls steadily till $t \sim 1500 \text{ d}$, which cannot be ascribed to a resolution effect, but rather reflects the decreasing asymmetry in brightness illustrated in Fig. 6. The $l = 2$ amplitude shows a sharp rise at $t \sim 500 \text{ d}$ which reflects the development of eastern and western hot spots discussed further in § 3.4 below. At

late times the amplitudes of $l = 1, 2$ and 3 are comparable, reflecting the increased complexity of the images.

3.2. Uncertainty in the Images

In order to discuss the images in detail, we first elaborate on the brightness uncertainty in them. The simplest estimator of this uncertainty is the standard deviation of the brightness in empty regions of the image, which we will call σ_{bg} , and which we list for each image in Table 1. However, for the reasons detailed below, σ_{bg} is likely somewhat of an underestimate of the true brightness uncertainty (see also Perley 1999).

The true uncertainty will have three principal components: 1) the effect of the thermal noise, 2) the effect of residual calibration errors, and 3) the effect of instabilities or inaccuracies in the deconvolution process, which could also be described as the effect of incomplete u - v coverage, since in the case of complete u - v coverage, no deconvolution is necessary and therefore no such instabilities or inaccuracies will occur.

We will discuss each of these components in turn. The effect of the thermal noise, 1), will be random, will be uniform over the image, and will scale with the number and size of the telescopes, the bandwidth, and the observing time. It can be well estimated by σ_{bg} . Unfortunately, the effects of 2) and 3) are less predictable, and may correlate with the actual structure in the image. There is thus the possibility that the effective uncertainty in our images over the extent of SN 1993J is higher than σ_{bg} .

The effect of residual calibration errors, 2), will be approximately proportional to the total flux density. We can estimate this effect as follows. Let N be the number of antennas, σ_ϕ be the rms of the residual phase mis-calibration in radians, and M be the number of independent time intervals. We will conservatively take M to be the number of hours of observing time to allow for correlated, slowly varying calibration errors. In our phase-referenced, and in some cases additionally phase self-calibrated data, the residual calibration phase errors, σ_ϕ are almost certainly $< 0.5 \text{ rad}$. We do not separately calculate the effect of residual amplitude calibration errors, since they are almost certainly smaller. Perley (1999) gives an estimate of the dynamic range limit due to residual mis-calibration of \sqrt{MN}/σ_ϕ , where the dynamic range is the image peak brightness divided by σ_{bg} . For our data, with $M \gtrsim 10$ and $N \gtrsim 11$, this gives a dynamic range of $\gtrsim 60$. This is probably a lower limit, since our phase-referencing cycle time was much shorter than 1 hour, and thus a realistic value of M is likely larger than 10. Since the observed dynamic range is smaller than this conservative limit for all except the earliest epochs, for which σ_ϕ is almost certainly less than 0.5 rad due to the high signal-to-noise ratio and accurate phase self-calibration, we can conclude that the uncertainty introduced by residual calibration errors is likely small.

The effect of 3), instabilities or inaccuracies in the deconvolution process, will be largely confined to the area over which CLEAN components were sought in the deconvolution process, in other words over the CLEAN window. The effect will scale with the completeness of the u - v coverage. We estimated the effect of the instabilities or inaccuracies in the deconvolution as follows: for a typ-

ical u - v data set, the actual, measured, visibilities were replaced by the Fourier transform of the SN 1993J image. A realistic amount of random noise was added to this artificial data set, which was then deconvolved. This process was repeated for many realizations of the random noise. We then computed the rms variation over the different noise realizations at various locations of the resulting images. For the 8.4 GHz data sets at $t = 264$ d, 451 d, 1693 d and 2525 d, the standard deviation of the brightness within the CLEAN window was higher by 20%, 33%, 16%, and 37% respectively, than that of the background.

We thus estimate the total image uncertainty in the CLEAN window, i.e., over the radio shell, to be between 1.2 and 1.4 times σ_{bg} , or the standard deviation of background brightness, the values of which are listed in Table 1.

3.3. Early Structure in the Shell and Apparent Rotation between 175 and 686 Days

The earliest 8.4 GHz image of SN 1993J, at $t = 50$ d, shows an almost unresolved source with a radius of just 0.14 mas or 520 AU, only 100 to 200 times larger than the radius of the progenitor star. No brightness structure can yet be seen. As mentioned above, the shell structure first becomes visible at $t = 175$ d. Already at this epoch there is a distinct asymmetry in the brightness, with a maximum to the east-southeast of the center and a minimum to the west. To make the asymmetry more visible, we display in Figure 8 the image at this epoch with a moderate degree of super-resolution, achieved using maximum entropy deconvolution as implemented in the AIPS task VTESS, which generates less spurious structure than CLEAN (Briggs 1995).

As the supernova expands, our relative resolution increases and the pattern of modulation of the ridge brightness becomes clearer. The pattern also appears to rotate counter-clockwise. By $t = 520$ d, the brightness peak is to the south and the gap to the north. In Figure 9 we plot the relative brightness, averaged radially from 0.7 to $1.0\theta_0$, as a function of p.a. for several early epochs. The p.a. of the gap clearly changes with time. The most consistent evolution is for the period between $t = 264$ d and 520 d, for which the gap moves from p.a. = 250° to 375° . The peak is at p.a. = 100° at $t = 264$ d and moves to p.a. = 180° by $t = 451$ d. To further illustrate this evolution, we plot in Figure 10 the p.a.s of the peak and the gap in the ridge as determined from the images for the period $t = 175$ d to 635 d. This figure shows that the apparent rotation is not uniform. It is more pronounced for the gap, which moves consistently counter-clockwise by $\sim 130^\circ$ between $t = 264$ d and 390 d. The peak rotates clockwise by $\sim 50^\circ$ between $t = 390$ and 451 d, and tends to rotate slightly counterclockwise at other times. We discuss the possible cause of this apparent rotation in §6.3 below, but we note here that it is possible that the apparent rotation is caused by a steady increase in brightness at p.a. of about -110° , and an unrelated decrease at p.a. $\sim 180^\circ$. In other words the brightness at different p.a.'s may be evolving independently, albeit with a timescale on the order of 200 d, and the appearance of a rotation coincidental.

What is the significance of the apparent rotation? The apparent rotation is also suggested at 5 GHz where the first resolved image at $t = 352$ d shows a very similar pattern, in particular having the same orientation as that at

8.4 GHz. From there on, the p.a.s of the peak and the gap at 5 GHz track those at 8.4 GHz well (see Figure 2).

More generally, we can assess the significance of changes apart from homologous expansion between images of SN 1993J at different epochs by scaling the images to the same effective size, and then comparing the remaining differences between the images with the image uncertainty. We find that the differences between the 8.4-GHz images at $t = 264$ d and 451 d, when appropriately scaled in size and flux density and then convolved to the same resolution, are six times the combined σ_{bg} . This apparent rotation thus represents a quite significant change in structure even with the conservative assumption of an uncertainty of $1.4\sigma_{\text{bg}}$ discussed in the previous section.

3.4. Development of Three Hot Spots Along the Ridge from 686 Days to 1253 Days

As the radio shell expands further, our relative resolution increases, and more complex structure becomes visible. The opening in the ridge narrows and the simple pattern with a single peak and gap gives way to an almost closed shell structure with an evolving, complex modulation along the ridge. In particular, starting at $t = 774$ d, the southeastern hot spot splits into an eastern and a southern one, and gaps appear to the north and the southwest. At $t = 1253$ d a large arc has developed stretching over about 150° in p.a., from the northeast to the south. During the same period, a third hot spot develops in the east, but in contrast to the other two hot spots, this hot spot remains stationary.

3.5. The Filling of the Northern Opening in the Ridge from 1253 Days to 3345 Days

From $t = 1253$ d on, the northern opening of the ridge begins to fill in. By $t = 1693$ d the original opening has essentially vanished, and from $t = 2064$ d on the original opening has brightened to the extent that it becomes a hot spot. By $t = 2432$ d, there are again three hot spots, a prominent one slightly east of north and ones in the west-southwest and south-southeast. At 8.4 GHz the dynamic range has decreased to ~ 10 for the last two epochs, at which level the brightness modulations along the ridge can no longer be discerned in detail. However, the pattern of modulation can be seen also in the 5.0 and 1.7 GHz images which have a higher dynamic range. Our latest image, at $t = 3345$ d and 5 GHz still exhibits the hot-spots to the west-southwest and the south-southeast. The hot-spot east of north is also still present, but has broadened somewhat.

Given the complexity of the structure, and the decreasing dynamic range of the images, it may not necessarily be apparent which features in the late-epoch images are real, and which are merely due to noise. Since we found in Papers I and II that the projection of a uniform spherical shell, with a shell thickness of 20% of the outer radius, was a good overall description of the supernova, we will examine the deviations of our images from such a model in order to illuminate the significance of the features in the images. As an example, in Figure 11, we show again our images for $t = 1893$ d at 8.4 and 5.0 GHz in grayscale, with contours showing the significance of departures from a spherical shell. More precisely, the contours represent the de-

viations from the projected, convolved uniform spherical shell model of the image, in units of σ_{bg} .

There are significant deviations from a uniform, spherical shell: $5\sigma_{\text{bg}}$ and $9\sigma_{\text{bg}}$ at 8.4 and 5.0 GHz respectively. Note that while the deviations at 5.0 GHz are more significant due to the higher dynamic range at that frequency, they are not larger, that is the supernova is not more uniform than at 8.4 GHz. Note also that even features with significance less than $3\sigma_{\text{bg}}$ may well be real since the addition of noise will not cause the disappearance of features at low amplitudes. In this example, as in the other images, there is excellent correspondence between the significant features at the two frequencies, in particular in this case for the opening to the northeast and the brightening to the southwest.

The CLEAN deconvolution process is subject to a known tendency to introduce small scale corrugation into the images (Cornwell & Braun 1988). To test to what extent this tendency might be responsible for the structure in our images, we made a biased image, again for $t = 1893$ d at 8.4 GHz, by deconvolving with maximum entropy (Cornwell 1988, 1999) using a default image consisting of the relevant projected uniform spherical shell. Even in this image, which has a relatively low dynamic range, and is biased to be as close to the uniform shell as is allowed by the data, there are deviations from a uniform shell of up to 25%, or $5\sigma_{\text{bg}}$, at 8.4 GHz. Even at this relatively late time, then, there are significant brightness deviations from a uniform spherical shell.

3.6. Polarization of SN 1993J

Synchrotron radiation is inherently polarized (e.g., Pacholczyk 1970), and the polarization properties can potentially reveal the magnetic field geometry. The integrated polarization of SN 1993J is low, being $< 1\%$ at centimeter wavelengths, as determined from some of our VLA observations (described Paper II). Because of the high degree of circular symmetry, however, it is possible that the polarization in a resolved image would be much higher.

In order to determine the polarization, observations in both senses of circular polarization are required, which we obtained for all our VLBI observing sessions after $t = 774$ d, with the exception of the one at $t = 1107$ d (Paper II). We did not detect any linear polarization larger than the expected antenna polarization leakage of a few percent in any of these VLBI sessions.

We carried out the full polarization calibration for several runs, namely those of $t = 1356$ d at 8.4 GHz, of $t = 873$ d, 2064 d at 5 GHz, and of $t = 3164$ d at 1.7 GHz. These runs were chosen because the images had high dynamic range, and consequently are the best choices for the search for polarization. To correct for the polarization leakage of each antenna, we determined the instrumental polarization parameters from our observations of M81*, which has very low intrinsic linear polarization (Brunthaler et al. 2001) and is thus an ideal instrumental polarization calibrator.

In no case did we find any significant polarization for SN 1993J. We give the results in Table 2. In no case did

we observe linear polarization greater than the 3%⁶ upper limit on the average polarization of the bright part of the ridge is 4.4% and on polarization at the image peak 9%.

4. A TIME-AVERAGED IMAGE OF SN 1993J

Our last five 8.4-GHz images in Figure 2 were convolved with a CLEAN beam of FWHM 1.12 mas. This is a somewhat lower resolution than the ~ 0.7 mas obtained in the imaging process as described in § 2. However, their relatively low dynamic range made it less useful to display them at the full resolution. A higher dynamic range, which would allow higher resolution, could be achieved by properly averaging the images. We showed in Paper II that the visibility curve of the radio shell, after scaling according to the expansion, shows only small changes with time over the time interval from $t = 996$ d to 2787 d. Since the radial profile of the radio shell is the Hankel transform of the visibility curve, this indicates, independent of any model-fitting and deconvolution, that the average radial profile also shows only small changes with time. Thus it is reasonable to average our data in time, accounting of course for the overall expansion. Such averaging allows us to study those characteristics of the radio shell which don't change over the averaging interval with higher angular resolution.

We accordingly averaged the data from the three latest epochs at 8.4 GHz to increase our dynamic range and form an image. This image will be an average over the three individual epochs, and we note that in the presence of changes from epoch to epoch, some deconvolution errors will be incurred. Since, however, both the changes from image to image and the sidelobes are only a fraction of the surface brightness, such errors should be no more than a few percent of the brightness. Nonetheless, specific small-scale features in the composite image should be interpreted with caution.

To produce the composite image, we scaled and averaged the data from the 8.4-GHz observing sessions at $t = 2080$ d, 2525 d, and 2787 d. To account for the expansion of the radio shell, we normalized the u - v distances by scaling them by the outer radius of the fit shell, normalized to the value at $t = 2787$ d (4.49 mas; see Paper II). For example, if the supernova was $1.5\times$ smaller than at $t = 2787$ d, the u - v distances would be divided by 1.5. We further scaled the magnitudes of the complex correlation coefficients by the respective total flux density for each epoch, and shifted their phases so as to place the center of the fit shell at the phase center. The combined data set was then imaged and deconvolved as usual. The result is shown in Figure 12. The increased dynamic range allows us to usefully image at the higher resolution of 0.7 mas. The shell appears very circular, but somewhat more uniform than it does in the individual images (Fig. 2). However, the brightness still varies by a factor of ~ 2 between the brightest and the faintest portions of the ridge. These variations represent changes of $\pm 4.5\sigma_{\text{bg}}$, with the rms variation of the brightness around the ridge being $2.2\sigma_{\text{bg}}$. We estimated the errors in the deconvolution in the same way we did for individual epochs in §3.2 above,

⁶ The linearly polarized flux density, S_{pol} , is $\sqrt{Q^2 + U^2}$ where Q and U are the measured Stokes parameters. By definition, S_{pol} is positive, and in the presence of noise is therefore biased. This bias has been calculated (Wardle & Kronberg 1974), and a bias correction has been implemented in the AIPS task COMB, which we used to calculate our linearly polarized flux densities. This procedure produces the correct mean value of S_{pol} , at the expense of occasionally producing unphysical negative values.

and found that the uncertainty is somewhat higher in this case: $1.7 \sigma_{\text{bg}}$. The reason for the higher uncertainty is that the u - v coverage is less dense at the largest u - v distances, which are given higher weight in this image. Despite the higher uncertainty, we find that the variation of the brightness around the ridge is significantly larger than the noise. In other words, there are likely true brightness contrasts of $\gtrsim 1.4$ in the bright part of the ridge which persist over periods > 1 year.

We can also use this image to calculate the circularity of SN 1993J, as we did for the individual images in Paper I. The axis ratio of an ellipse fit to the 20% contour is 1.01. The rms variation over all p.a.'s of the radius of the 20% contour is 4%. These values are consistent with those we reported in Paper I. We note here that the 8.4 GHz image at $t = 2787$ d and the 5.0 GHz images are circular to similar limits as reported for the earlier 8.4 GHz images in Paper I. On the latest image, at $t = 3345$ d (5.0 GHz), an ellipse fit to the 20% contour has an axis ratio of 1.06 (at p.a. = 76°). This is within the uncertainty for the average ellipticity reported in Paper I, but somewhat larger than those obtained at other recent epochs. Perhaps this is an indication that SN 1993J is becoming elliptical. Future measurements will be required to confirm whether this is the case.

Does the radius variation in the outer contours reflect small-scale departures from circularity, or is it due only to noise? To determine this we performed a Monte-Carlo simulation, substituting the Fourier transform of a circularly symmetric model for the composite set of visibilities above. We then added a realistic amount of noise to these model visibilities and imaged them. Over numerous realizations of the noise, we found that the average rms variation over all p.a.s of the radius and the average ellipticity of the 20% contour were not significantly different than found for the real data. The 1σ upper limit on the rms variation of the 20% contour radius not due to noise is 3%. We thus find no indication that the wavyness of the outer contours represents any significant deviation from circularity.

There is, however, a small protrusion visible to the southwest on the composite image. At the 16% contour, it extends about 0.6 mas beyond the average radius. It has a flux density of $\sim 0.5\%$ of the total, equivalent to $\sim 6 \sigma_{\text{bg}}$. There may be further, similar protrusions, but with lower brightness, and therefore not distinguishable from the noise. Is this protrusion visible in the individual images? It is indeed apparent in the 8.4 GHz images at $t = 2080$ and 2525 d. At 5 GHz, it is visible in the image at $t = 2432$ d, not in the one at $t = 2996$ d and only suggested in the last one at $t = 3445$ d. It is not apparent in the latest 1.7-GHz image at $t = 3164$ d (Fig. 4), but we might not expect it to be, given the lower resolution at that frequency. The protrusion is suggestive, but its reality will have to be established by future observations.

5. THE RADIAL BRIGHTNESS PROFILE

It is of considerable interest to determine the average radial brightness profile of the supernova. The observed profile provides an important constraint for modeling the shell structure, the density profiles of the ejecta, and the

emission and absorption processes. To study the profile of SN 1993J with the highest angular resolution we used the composite image in Figure 12, and produced a profile of brightness *vs.* radius, which we plot in Figure 13. The uncertainties in the profile were derived from the larger of σ_{bg} and the rms scatter with position angle within each radial bin, both divided by the square root of the number of beam areas within each bin.

In addition, we plot the profiles of the models. We used a spherical shell of uniform volume emissivity as a model for our u - v fits in Papers I and II. The radial profile of that model, fit to the present composite data set is indicated by the dotted lines in Figure 13. The fit toward the outer edge of the profile is excellent, indicating that our model is good at least to the limit imposed by the resolution.

In fact, the true radial profile of SN 1993J is not expected to precisely follow this form (see e.g., Mioduszewski et al. 2001; and Jun & Norman 1996a, 1996b). We noted in Paper II (as did Mioduszewski et al. 2001) that toward the center of the shell, the observed profiles show systematic deviations from that of a spherical shell of uniform volume emissivity. Specifically, Figure 13 shows that, from the maximum inward, there is a deficit in emission toward the inside of the ridge and then an excess in the center. A thicker shell would provide a better fit on the inside of the ridge, but a worse fit in the center of the shell. The deficit in the center can in general also be seen in our well-resolved images at both 8.4 and 5 GHz, for example those shown in Figure 11, where the deficit in the center is still $> 4 \sigma_{\text{bg}}$ even in the biased maximum entropy image.

We will use the above scaled and time averaged data set from $2080 \text{ d} \leq t \leq 2787 \text{ d}$, which was used to make the time-averaged image discussed in § 4, to quantify these differences and to better determine the real shell emission profile. We will do this by again directly fitting the u - v data as described in Papers I and II. We note that by fitting directly to the u - v data, we avoid deconvolution errors so that our fit profile is a correct representation of the time-averaged profile of the supernova. Since the most prominent difference between the model and our data seems to be a deficit of emission in the center of the shell, we add a uniform disk of *negative* emission to our previous model of the projection of an optically-thin, uniform spherical shell. The physical motivation for this parameterization, in particular for the negative emission, is to represent possible absorption in the interior of the shell, which might be expected on physical grounds (e.g., Mioduszewski et al. 2001). Such absorption would lower the brightness in the central region of the projected supernova by absorbing some of the flux from the rear of the shell. Complete absorption in the interior of the three-dimensional shell would imply a reduction of exactly one-half the brightness in the central region, corresponding to a negative emission disk whose brightness was the negative of the observed average brightness in the central region. The disk and the shell have the same center, but the radius and the total (negative) flux density of the disk are free parameters⁷.

We find that the best fit of the modified shell model gives a shell thickness of 0.25 times the outer radius θ_0

⁷ We note that a disk is only an approximation to the profile expected for absorption in the interior of a three-dimensional shell. The approximation is reasonable when, as in our case, the radius of the absorbing material is well within the outer radius of the shell.

(equivalent to $\theta_o/\theta_i = 1.34\theta_o$), a radius for the absorption disk of $0.5\theta_o$, and an absorption of 4% of the total flux density. The absorption corresponds to a reduction in the brightness of $\sim 25\%$ near the center of the shell. The radial profile of this model is shown by the solid line in Figure 13. The inclusion of an absorbing disk in the center allows a slightly thicker shell to better fit the inner profile of the ridge without an excess of emission in the center of the shell. There are still some deviations of our measurements from the model profile, especially near the center. The resolution, however, is 0.70 mas ($0.15\theta_o$), and therefore the several points nearest the center which still show a deficit compared to the model are highly correlated and probably not significant.

We repeated this analysis with the 5 GHz data sets of $t = 2992$ and 3345 d, and found a very similar result: the best fit of the modified shell model gives a shell thickness of 0.25 times the outer radius θ_o (equivalent $\theta_o/\theta_i = 1.33\theta_o$), a radius for the absorption disk of $0.4\theta_o$, and an absorption of 4% of the total flux density. At 5.0 GHz, the fit radius of the absorbing disk is somewhat smaller than at 8.4 GHz. For reasons we will elaborate on below, however, the parameters of the absorbing disk should be interpreted with caution.

In fact, at this early stage, the inner ejecta are still expected to be quite opaque to radio waves (Chevalier 1982c; Reynolds & Chevalier 1984; Mioduszewski et al. 2001), and we might reasonably expect almost complete absorption of the radio emission from the rear of the shell. Accordingly, we fit also a model with an absorbing disk representing complete absorption and with a radius equal to the inner radius of the shell. In this case, the fitted shell thickness is $0.35\theta_o$. This model is also plotted in Figure 13, using a dashed line. It clearly provides a poorer fit than the model with the fitted absorption.

What is the uncertainty in the fit shell thickness? The formal uncertainty on the shell thickness when an incomplete absorption disk is also fit is $0.03\theta_o$. This uncertainty is derived directly from the visibility data, and therefore is not affected by the higher on-source errors in the image plane discussed in § 3.2 above. Since, however, our fit uses an approximation to the geometry of an absorption disk, and since the geometry of the absorption probably differs from a simple disk, our formal uncertainty may somewhat underestimate the true uncertainty in the shell thickness⁸. In any case, the fits without any absorption disk and with a complete absorption disk are clearly worse, suggesting that a very conservative range for the true shell thickness is between $0.23\theta_o$ and $0.35\theta_o$.

A more model-free estimate of the shell thickness can be derived from the measured radial profile. A three-dimensional shell emission region, whose radial profile has sharp boundaries at θ_i and θ_o like any of our three models in Figure 13 will, when projected onto two dimensions, have a radial profile with inflection points at θ_i and θ_o . Convolution with the CLEAN beam will smooth these inflection points. If we assume that extrema in the second derivative of the convolved profile trace the location of un-convolved inflection points, then these extrema occur at the projected inner and outer radii of the shell. We

determined the extrema of the second derivative from our measured profile in Figure 13 numerically, and their locations suggest a shell thickness close to the lower end of the above range, that is $\sim 0.23\theta_o$. In summary, we think that our fit value of the shell thickness of $(0.25 \pm 0.03)\theta_o$ is a reasonable estimate of the thickness of the radio shell.

6. DISCUSSION

With thirty-one epochs of observations of SN 1993J, phase-referenced to the core of the host galaxy, we produced sequences of images of the radio shell over more than nine years from the time of explosion to the present. In our Galaxy, radio shells of supernovae have been observed over at most $\sim 10\%$ of their age. SN 1993J has been observed essentially over 100% of its age. In the first paper of this series, we determined the position of the explosion center in the galactic reference frame with an accuracy of about 160 AU, and placed an upper limit of 5.5% on anisotropic expansion in the plane of the sky. In the second paper, we determined the deceleration of the expanding supernova as a function of time, together with the radio light curves and the spectrum, and interpreted our results in terms of the interaction of the ejecta with the CSM. In this third paper we focus on the details of the images of the evolving radio shell.

The earliest image shows an almost unresolved source with a radius of 520 AU. The shell structure can be discerned from $t = 175$ d on. The brightness along the ridge is modulated, with a maximum and a gap located almost opposite. This modulation pattern appears to rotate, with the gap rotating from the west to the north-northeast in the following 250 d. From then on the structure along the ridge becomes more complex. Even at our last few epochs, however, the outer contours of the (projected) radio shell remain circular within 4%. The brightness in the center of the shell is less than would be expected of a uniform, optically thin shell. With absorption in the center taken into account, the ratio of the shell thickness is $0.25\theta_o$. No significant linear polarization was found.

These results are important for discussions about 1) the origins of the brightness modulation of the shell and in particular, possible structure in the ejecta, Rayleigh-Taylor instabilities, structure in the CSM and a possible distant companion, and structure of the magnetic field, 2) the relation between the outer edge of the radio shell and the forward shock front, 3) a possibly non-uniform shell thickness, 4) absorption in the center of the shell, and 5) the possibility of discovering a pulsar nebula in the center of the radio shell. We discuss each of these aspects in turn.

We discuss our results in light of the theoretical understanding of the structure of an expanding supernova shell described in the introduction. This structure is expected to comprise a forward shock, driven outward into the CSM, and a reverse shock propagating inward in the expanding ejecta (see e.g., Chevalier 1982a). The CSM, in the case of SN 1993J, consists of the slow, dense stellar wind of the progenitor. The contact discontinuity between the shocked CSM and the expanding stellar envelope is located between the forward and reverse shocks. Radio emission is thought

⁸ Our uncertainty does take into account that the fitted shell thickness is highly correlated with the fitted radius and total absorption of the absorbing disk. However, the presence of correlated visibility errors, such as would arise from residual calibration errors, might also slightly increase the true uncertainty.

to be produced in the region between the forward shock and the contact discontinuity by particles accelerated by the shock and magnetic fields amplified by instabilities at the contact discontinuity. In the case of a decelerating shell, it is expected that the contact discontinuity will be Rayleigh-Taylor unstable (Gull 1973; Chevalier 1982a, b, c; Chevalier & Blondin, 1995), and that with time “fingers” of shocked envelope material will extend into the shocked CSM. The shear flow along the sides of these fingers makes them subject also to the Kelvin-Helmholtz instability, which may well further amplify the magnetic field (Jun & Norman 1996a, b). We expect these instabilities to apply to SN 1993J, which is already substantially decelerated (Paper II; see also Bartel et al. 2000, Marcaide et al. 1997, 2002). The magnetic field strength in SN 1993 can be estimated from its size or velocity and the synchrotron luminosity and spectrum (Paper II; Chevalier 1998; Fransson & Björnsson 1998). In fact, the magnetic field in SN 1993J is several orders of magnitude higher than that expected in the stellar wind, which led Fransson & Björnsson (1998) to argue that some form of field amplification must be occurring as even a strong shock will amplify the field only by a factor of four.

Many of the features of our images could be interpreted in a straightforward way within this scenario: the forward shock is at or near the outside boundary of the radio emission, and is highly circular. The contact discontinuity represents the inside boundary, and shows deviations from circularity due to instabilities which are visible chiefly as brightenings of the shell, rather than as actual fingers, due to projection and to our limited resolution. Numerical modeling has shown that the Rayleigh-Taylor fingers do not generally reach the forward shock (Chevalier, Blondin & Emmering 1992; Jun & Norman 1996a, b), and so the outer edge of the shell remains highly circular.

Our simple model of an optically thin, spherical shell of uniform volume emissivity can serve as a rough description of a supernova with this structure, with the inner and outer boundaries of the shell being, respectively, the forward shock and the contact discontinuity. Of course, the volume emissivity is not expected to be strictly uniform within this region (see e.g., Mioduszewski et al. 2001; Jun & Norman 1996a, b), but because even at the last epoch of our observations at 8.4 GHz our resolution is only comparable to the shell thickness, a uniform shell should provide an adequate first order description. However, our images clearly show deviations from this structure. We will discuss first the deviations of the azimuthally averaged profile (Fig. 13), and then the smaller-scale modulations of the shell brightness visible in the images (Figs. 2, 4, 12).

6.1. *Deficit of Emission in the Center of the Shell — An Opaque Interior?*

We found that our data show a deficit of emission in the center of the shell, and an excess just inside of the ridge peak when compared to the uniform spherical shell model with the best fit. A thicker shell would fit the ridge profile better, but produce an even brighter central region. We parameterized the deficit in the center by fitting a disk of negative brightness in addition to the spherical shell (§5), and we found a deficit of $\sim 4\%$ of the total flux density, occurring over a radius of about half of the outer radius of the shell, θ_0 .

There are a number of reasons why such a deficit might be expected for SN 1993J, and below we discuss several of them, which are not mutually exclusive. An obvious one would be that SN 1993J be intrinsically non-spherical, for example prolate, and that we observe it face on. However, since the outer contours are highly circular, the prolate structure would have to be aligned with the line of sight to within a few degrees. If we assume that the apparent deficit of emission in the center is entirely caused by SN 1993J being in fact prolate, the chance of an alignment close enough to the line of sight so that SN 1993J would still appear as circular as it does is $< 5\%$. Such a coincidence is unlikely. Moreover, such an orientation is hard to reconcile with the optical polarization data, which imply that we are *not* seeing SN 1993J along an axis of symmetry (Trammell et al. 1993; Tran et al. 1997; see also Höflich et al. 1996).

An equally obvious reason would be that the shell thickness is different for different parts of the shell. A shell which was thinner, or had lower volume emissivity, at the front and/or rear than it did along the circumference of the projected shell would produce the observed deficit. Once again, this would require a coincidental alignment with the line of sight. In view of the other plausible explanations for the central deficit, we do not consider these two possibilities further.

A third geometric explanation would be a shell which is in fact thinner than the 25% of its outer radius derived in §5, but which is “dimpled”, having local displacements from the average radius. In the center, a thinner shell seen in projection would produce relatively lower brightness. Near the limb, the dimpling seen in projection would produce an apparently thicker shell on average. Such a geometry is not unlikely given the expected Rayleigh-Taylor instability of the contact surface.

A fourth possibility is that the magnetic field is predominately radial, as is expected if field amplification occurs due to instabilities at the contact discontinuity (Jun & Norman 1996a, 1996b), and as is observed in older remnants (Milne 1987; Dickel, van Breugel, & Strom 1991). In this case even a spherical shell will show enhanced emission along the limb because the magnetic field at the limb will lie predominately in the plane of the sky, and the synchrotron emission is strongest in directions perpendicular to the magnetic field. The polarization observations would appear to contradict this scenario, since a well-ordered field should produce high polarization which is not observed. However, as we argue below, internal Faraday rotation is likely to depolarize any centimeter wavelength radio emission.

Finally, the most probable explanation is that significant absorption in the interior of the shell is attenuating the emission from the side away from us. In fact, at this early stage, the inner ejecta are still expected to be opaque to radio waves (Chevalier 1982; Reynolds & Chevalier 1984; Mioduszewski et al. 2001) because of their high densities. Only if the inner ejecta have become transparent by filamentation (Bandiera, Pacini, & Salvati 1983) are we likely to be able to see any emission from the distant side of the shell in the first several decades after the explosion.

When we fit an absorbing disk to our data in addition to the spherical shell, we found that the disk absorbed only

4% of the total flux density and had a radius of roughly half the outer radius of the shell, θ_o . If the region inside the reverse shock were completely opaque, one would expect an absorption of $\sim 25\%$ of the flux density, occurring over the inner radius of the shell or $0.75 \theta_o$. Even complete absorption over the fitted radius of the absorbing disk would result in 9% of the flux density being absorbed. Thus, taken at face value, our fit of the absorption disk suggests incomplete absorption over a region well within the reverse shock, possibly implying filamentation of the inner ejecta.

Complete absorption at the inside radius of the shell would result in a drop of 50% of the surface brightness at the projected inner radius or θ_i . Even with our limited resolution, this would produce a steep drop in the profile to the inside of the ridge line, as can be seen in the complete absorption model profile in Figure 13 (dashed line). The profile of that model is too steep on the inside of the ridge-line. In fact, even if we modify the shell profile so that the volume emissivity of the shell is 0 at the inner radius, and rises linearly to the outer radius, in other words, to soften the slope inside of the ridge line as much as possible, the model profile does not fit the observed one. This profile is plotted in Figure 14 (dotted line).

We conclude that if there is complete absorption in the interior of the shell, then the outer edge of the absorbing region must be somewhat soft, or that the optical depth near the inside edge is still small, and it rises only gradually towards the center of the shell. We plot such a model in Figure 14 (solid line). We note that this model is not unique. Rather than varying the optical depth, or the opacity as a function of the radius, we vary the fraction transmitted through the interior of the shell. It seems likely that this variation in effective opacity is due to mixing, being more properly described as a variation in the filling factor of the opaque material, in which case our treatment is reasonable.

However, the other mechanisms discussed above may also modify the brightness. Furthermore, a non-uniform volume emissivity in the shell would also alter the apparent absorption derived by fitting a uniform shell. A more quantitative determination of the emission and absorption profile will have to wait for higher relative angular resolution and the development of more sophisticated u - v plane models. In summary we believe some absorption in the interior of the shell is strongly suggested by the data. Complete absorption in the center of the shell is compatible with our data, however, complete absorption everywhere inside the inner shell radius is not.

6.2. *Does the Outer Edge of the Radio Shell Coincide with the Forward Shock?*

How is the outer edge of the radio shell related to the forward shock front? One would expect the radio emission region to be bounded on the outside by the forward shock, which is principally responsible for accelerating the electrons which produce the radio emission. However, since the magnetic field, also necessary for synchrotron emission, is thought to be principally generated by amplification occurring near the Rayleigh-Taylor unstable contact

interface, it is possible that the effective radio emission turn-on is significantly inside the forward shock (e.g., Jun & Norman 1996a). Therefore the radio emission itself can only indirectly reveal the location of the forward shock. Nonetheless, our radio images do give some suggestions concerning both geometry and location of the forward shock.

First, Mioduszewski et al.'s (2001) hydrodynamical modeling of SN 1993J gives a distance between the inner and outer shocks of $\sim 20\%$ the radius of the outer shock⁹. Our measured value of the radio shell thickness of $25 \pm 3\%$ of the outer radius is somewhat larger. It seems unlikely that the radio emission originates either inside the reverse shock or outside the forward shock. It therefore seems most plausible that the location of the forward and reverse shocks do indeed coincide closely with θ_o and θ_i .

Second, the projection of the radio shell has remained remarkably circular from the earliest observations to the present. We determined an upper limit to deviations from circularity of 5% for the radio shell from $t = 30$ d to 90 d (Bartel et al. 1994) and of 3% for later times (Paper I; this paper), despite the significant modulations of the brightness along the ridge. The outer radius of the model radio shell is very well determined and evolves very smoothly as a function of time (Paper II). These characteristics suggest that, at least on average, the outer edge of the radio shell is not influenced by local peculiarities of the brightness distribution but determined by a fundamental parameter of the expanding supernova. It also suggests that the forward shock, like the outer edge of the radio shell, is very circular in projection, since it would be unlikely that any radio "turn-on" distance varies so as to make the radio outer edge circular when the shock front is not.

Is the outer radio turn-on sharp? Our model of a spherical shell with uniform volume emissivity produces an excellent fit, especially near the outer edge, to the projected brightness distribution (see Figure 13, Paper II). A distribution of volume emissivity that drops sharply at the outer edge of the shell is therefore consistent with our data. However, a sharp outer edge to the three-dimensional radio shell is not required by our data, since our resolution is only comparable to the shell thickness. Specifically, a model in which the volume emissivity is maximal at the inner radius of the shell and then decreases linearly to zero at the outer radius can be made consistent with the observed radial profile from the maximum outwards. The limited resolution and projection onto the sky render the recovery of the details of the distribution of volume emissivity virtually impossible. Future observations with a higher relative resolution will be required to determine the details of the variation of volume emissivity in the shell.

Comparison of the optical expansion velocities with the expansion velocity determined from the radio observations could shed further light on the relation between the outer edge of the radio emission and the forward shock. We will discuss this subject in more detail in a forthcoming paper (Paper IV).

⁹ The self-similar solutions of Chevalier (1982a) also predicts a shell thickness, and give a thickness of 23% for the values of $m = 0.83$ and an external density $\propto r^{-2}$, typical for a few years after the explosion (Paper II). The predicted shell thickness varies only weakly for different m (Chevalier & Fransson 1994). However, since we showed in Paper II that the evolution is not self-similar, it is possible that the shell thickness may vary systematically from that determined by Chevalier.

6.3. *The Origins of the Brightness Modulation of the Shell*

The brightness along the ridge of the projected shell is substantially modulated at all epochs. Even in our time-averaged image from $2080 \text{ d} \leq t \leq 2787 \text{ d}$, the brightness varies by a factor $\gtrsim 1.4$. This variation in the brightness of the projected shell implies an even larger variation in the volume emissivity of the radio shell. There are a number of possible causes for this variation. We will discuss in turn the four most likely causes and assess their relevance to the structure apparent in our images and to its evolution in time.

1. *Structure in the ejecta.* Any structure in the supernova ejecta, for instance clumping or velocity anisotropy, could cause a modulation of the brightness in the radio shell. Recent numerical studies (see Müller, Fryxell, & Arnett 1991; Fryxell 1994; Burrows, Hayes, & Fryxell 1995) suggest that the ejecta in type II supernovae develop strong hydrodynamic instabilities even before shock breakout, just minutes after core collapse. The linear polarization found in the optical emission (Trammell et al. 1993), and perhaps also the asymmetry found in the optical lines (Lewis et al. 1994; Spyromilio 1994), suggest asymmetry in the ejecta for SN 1993J. Aspherical models for the ejecta were suggested to account for the optical polarization. In particular, oblate models with a major to minor axis ratio as large as 1.7 could explain the polarization results. The brightness distribution in our early radio shell images is strikingly aspherical. Perhaps this asphericity was caused by structure in the ejecta.

Evidence for fragmented ejecta has been found in several Galactic and extragalactic supernova remnants, including Cas A (Braun, Gull, & Perley 1987; Anderson et al. 1994), Tycho (Seward, Gorenstein, & Tucker 1983) and Kepler (Bandiera & van den Bergh 1991), all of which have remained relatively circular in overall appearance despite the fragmentation of the ejecta. Numerical simulations by Cid-Fernandes et al. (1996) show that the fragmentation of the ejecta is a continuing process, with progressively smaller clumps forming in the first few years as the supernova expands. There is some observational evidence for the existence of clumping in the ejecta of SN 1993J (Filipenko, Matheson, & Barth 1994; Spyromilio 1994; Wang & Hu 1994).

The $l = 1$ (see §3.1) modulation seen at early times, however, cannot easily be explained by fragmentation, which is expected to occur on scales small compared to the shell diameter. Furthermore if anisotropy in the ejecta did occur on scales of the shell diameter, we would expect a non-circular shell, which is contrary to our results. Such fragmentation in the ejecta may, however, be the cause of the smaller-scale clumpiness seen in the radio shell at late times. The modulation of the shell brightness due to the fragmentation in the ejecta would likely expand with the shell, with a modulation pattern changing only slowly with time. Such a slowly changing structure is indeed observed in our sequence of images after $t \sim 1500 \text{ d}$.

2. *Rayleigh-Taylor instabilities.* Instabilities in the expanding shell will produce a modulated shell brightness. As mentioned above, the contact surface between the ejecta and the CSM is expected to be Rayleigh-Taylor un-

stable. Theory suggests that the growth of the instability be such that small fingers appear first and larger ones later (Gull 1973; Chevalier 1982c). This suggestion is supported by the numerical work of Jun & Norman (1996a, b), who also find that the scale of the Rayleigh-Taylor fingers is small in comparison to the shell diameter. As with fragmentation of the ejecta above, modulation of the shell brightness on the scale of its radius is unlikely. This instability is also expected to grow with time. Therefore this mechanism is unlikely to explain the prominent $l = 1$ modulation seen at early times. By contrast, the growing amplitude and decreasing relative scale size expected of the instabilities at the contact surface are a good match for the modulation seen at late times.

Could the possible protrusion seen in the last images be a Rayleigh-Taylor finger, protruding beyond the outer shock? As we mentioned earlier, the fingers are generally not expected to reach the outer shock front (Chevalier, Blondin & Emmering 1992; Jun & Norman 1996a, b). However, Jun, Jones, & Norman (1996) showed that a clumpy exterior medium enhances the growth of the Rayleigh-Taylor fingers, and allows a few fingers to grow enough to penetrate the outer shock. It is not clear, however, that such penetration could occur within the first decade. Future observations will show whether the protrusion is, in fact, real, and whether it continues to grow.

3. *Structure in the CSM and a possible distant companion.* The structure in the shell could also be due to pre-existing structures in the CSM, which will generally influence the shell brightness more directly than by enabling the growth of a few Rayleigh-Taylor fingers beyond the shock front as discussed above. (See Jones et al. 1998 for a general discussion of the effect of the CSM on an expanding supernova). In fact, in SN 1993J, we have a unique probe of the nature of the CSM of an evolved star. Clumping in the external medium has been invoked to explain the radio light-curves of SN 1993J (Van Dyk et al. 1994), although Fransson & Björnsson (1998) have fit the radio light-curves without resort to clumping. Although the origins of possible clumps in the stellar wind are not well known, it seems likely that the clumps would form at the stellar surface with scales $\ll r_{\text{star}}$, and that the clumps would then tend to dissipate as the wind flows outward, since the sound-speed in the wind is comparable to its expansion velocity. Thus one would expect the structure produced by a clumpy wind to scale in size and diminish in intensity with distance from the progenitor, and be characterized by $l > 1$ modulation.

Could structure in the CSM be responsible for the $l = 1$ modulation seen early on, and in particular for the apparent rotation of the modulation pattern between $t = 223 \text{ d}$ and 451 d (§3.3)? Blondin, Lundqvist, & Chevalier (1996) simulated the effect of a supernova expanding into a CSM which had an axisymmetric density gradient. Such a density gradient might result from a density distribution in the stellar wind which was axisymmetric about the progenitor's rotation axis. However, an axisymmetric pattern would produce an $l = 2$ rather than an $l = 1$ modulation.

To produce the apparent rotation of the modulation pattern we see, a roughly spiral pattern in the CSM would be required, with a size of $\sim 3000 \text{ AU}$. Given the different rotation of the brightness peak and gap, and the fact that the apparent rotation seems to have a beginning and an

end in time, a CSM geometry considerably more complex than a simple spiral would be required to account for the brightness modulation in detail. A possibility, albeit somewhat speculative, is that spiral structure in the CSM was produced by the colliding winds of a binary. The slow wind velocity of SN 1993J's progenitor of $\sim 10 \text{ km s}^{-1}$, along with the pitch of the spiral pattern, implies a long period for the binary of $\sim 6000 \text{ yr}$. This long period is not compatible with the close binary which probably stripped much of progenitor's hydrogen shell mass (Paper II), and therefore suggests a distant tertiary component to the progenitor system. We note that a dust plume with spiral morphology of roughly this size was recently seen near the red supergiant VY CMa by Monnier et al. (1999), who propose that it is caused by such a distant binary companion.

4. Structure in the magnetic field. The magnetic field structure in the CSM can also influence the synchrotron brightness of the shell, even in the absence of a significant density inhomogeneity. The magnetic field in the CSM is not expected to be dynamically important, and therefore not likely to deform the forward shock. The synchrotron emissivity, however, depends on the orientation of the magnetic field, being smallest when the field lies parallel to the line-of-sight. The orientation of the CSM magnetic field may thus influence the appearance of our images. Numerical studies (Jun & Jones 1999; Jun & Norman 1996b) have confirmed that the magnetic field orientation is important in determining the synchrotron brightness. In fact, the simulations of Jun & Norman (1996b) showed that the orientation of the weak external field, which is amplified by the forward shock, can have a significant impact on the synchrotron emissivity. A twisted field orientation, for example, might account for the peculiar apparent rotation of the brightness distribution seen between $t = 264$ and 451 d . At early times the field in the interaction region would still be dominated by the shock-compressed pre-supernova field, while at later times, it would become dominated by the component which has been amplified and also randomized by the combined Rayleigh-Taylor and Kelvin-Helmholtz instabilities. The field orientation might well contribute to both the early $l = 1$ and the late $l > 1$ modulation of the shell brightness.

What can the observed linear polarization tell us about the structure of the magnetic field? We observed low values for the polarization of the bright ridge of SN 1993J (§3.6), whereas the synchrotron emission from a region of uniform magnetic field is expected to be 70% polarized (e.g., Rohlfs & Wilson 1996). The low polarization of $< 3\%$ that we observed therefore suggests some source of depolarization, or a highly disordered field. Faraday rotation along the line of sight within the emitting region can cause depolarization of the radio emission even if the field is well ordered. Since the thermal electron densities and magnetic fields in SN 1993J are high, we might expect significant internal Faraday rotation. For our purposes here, the rotation measure, RM , can be taken as $RM = 810 n_e B L \text{ rad m}^{-2}$ where n_e is the thermal electron density in cm^{-3} , B is the magnetic field in mG, and L is the path length in pc. In Paper II we estimated the magnetic field at $t = 3000 \text{ d}$ to be $B \sim 5 \text{ mG}$ (see also

Fransson & Björnsson 1998, who obtain a higher value). The density can be estimated from the mass within the interaction region of $0.3 M_\odot$ (Paper II) and its volume calculated from our shell radii. For $t = 3000 \text{ d}$ we obtain a value of $n_e \sim 10^4 \text{ cm}^{-3}$. Armed with these estimates, we can calculate the path length which would cause a 2π rotation of the polarization vector at 8.4 GHz to be 10^{-4} pc . This path length is the scale on which the radio emission would become depolarized. It also is very short compared to the size of the supernova, corresponding to an angle of only $\sim 7 \mu\text{as}$ in our images. Clearly, we expect the relatively large magnetic fields and densities to highly depolarize any centimeter wavelength radiation merely due to line-of-sight depolarization. Although the RM will decrease as the supernova expands, the brightness and thus the signal-to-noise ratio will decrease also. Unless there is a strong separation between the thermal and the synchrotron-emitting relativistic particles, it is unlikely that useful polarized radio emission will be seen in the near future.

In summary, the brightness modulation in our images likely shows the effects of both the fragmentation of the ejecta and the Rayleigh-Taylor instability expected at the contact discontinuity. However, there also seems to be another source of strong modulation which is most significant at early times, in particular modulation with scales comparable to the radius of the shell, or $\sim 4000 \text{ AU}$. Given the high degree of circularity seen later on, the strong modulation of brightness at early times is unusual. Neither fragmentation of the ejecta nor the Rayleigh-Taylor instability is likely to produce such a modulation of the shell brightness. The most probable candidates are either density structures or an ordered magnetic field in the CSM.

6.4. A Pulsar Nebula?

SN 1993J is thought to have produced a compact remnant. Given the estimates of the progenitor mass, this compact remnant is probably a neutron star rather than a black hole, and the neutron star is generally expected to manifest itself as a pulsar. The strong relativistic wind of a young pulsar is expected to produce a bright, flat-spectrum synchrotron nebula. The expansion rate of such a pulsar nebula is expected to be $< 10\%$ that of the shell. Therefore even at our latest epoch the angular size of such a nebula would likely be $< 1 \text{ mas}$ (Reynolds & Chevalier 1984; Chevalier & Fransson 1992; Jun 1998). We find no such compact feature in our individual images (see Fig. 2). In particular, we examined a high-resolution image at $t = 2787 \text{ d}$, which had a convolving beam area of 0.48 mas^2 , and found no emission near the center brighter than $0.11 \text{ mJy beam}^{-1}$. We also do not find any such compact feature in our composite image from $2080 \text{ d} \leq t \leq 2787 \text{ d}$, where there is a deficit in the very center of the image, and the brightest feature in the central region represents only about $0.05 \text{ mJy beam}^{-1}$ for a beam area of 0.55 mas^2 . At 8.4 GHz and the distance of M81, the equivalent brightness of the ~ 950 -year-old Crab Nebula would be $0.15 \text{ mJy beam}^{-1}$. A seven-year-old pulsar nebula, on the other hand, is expected to be considerably brighter than one 950 years old (Bandiera, Pacini, & Salvati 1984), and should therefore be detectable in our images even if it were considerably less luminous than the

Crab. However, as mentioned above, the material in the center of the radio shell is likely to still have a high enough density so as to be opaque to radio waves (Chevalier 1982c; Reynolds & Chevalier 1984; Mioduszewski et al. 2001). The non-detection of the expected pulsar nebula therefore leads us to conclude that either the pulsar nebula is much weaker than the Crab, or that the material immediately surrounding the putative pulsar nebula cannot yet have become transparent by filamentation.

7. CONCLUSIONS

1. A sequence of VLBI images of SN 1993J at 30 epochs from $t = 50$ d to 3345 d shows the dynamic evolution of the expanding radio shell of an exploded star in detail.
2. The shell structure first becomes visible at $t = 175$ d, and is present in all subsequent images.
3. The brightness distribution changes significantly and systematically throughout the sequence of images. The evolution is clearly not self-similar.
4. At $t = 175$ d, the brightness around the ridge is significantly modulated, with a maximum or peak to the south-east and a minimum or gap to the west. Over the next 350 d, this pattern rotates counter-clockwise, although the peak and gap appear to rotate by slightly different angles and at slightly different times.
5. From $t = 774$ d to 1253 d, the gap fills in and three hot spots develop to the west, south and east.
6. From then on the northern part changes significantly. From $t = 2080$ d, hot spot develops in the north-northeast at the p.a. of the previous gap. There are also two further hot spots, one to the south-southwest and one to the west.
7. Throughout our observing interval, the brightness around the ridge of the projected shell is modulated by a factor of $\gtrsim 1.4$ on spatial scales of ~ 4000 AU (1 mas).
8. At early times, the modulation of the shell brightness on the scale of the shell radius is substantial, whereas at later times, the modulation on the scale of the radius is small.
9. Despite the modulation in brightness, even at our last epoch, we find no evidence that the outer contours of the projected shell deviate from circularity by more than a few percent. However, a first indication of a possible protrusion was found in our last images.
10. The radio emission of the bright part of the shell is $< 4.4\%$ linearly polarized. Internal Faraday rotation is expected to produce essentially complete depolarization.
11. The brightness in the central region of the projected radio shell is lower than that of a model with uniform volume emissivity in an optically thin, spherical shell. We consider absorption in the interior of the shell more likely than a non-spherical geometry with a thinner shell at the front and/or the back.
12. The outer edge of the projected shell accurately matches that of the above model, thus an emission volume with a sharp outer edge is consistent with our data.
13. The best fit value of the shell thickness, derived from model-fits to the 8.4 GHz $u-v$ data between $t = 2080$ d and 2787 d and by allowing for absorption in the center, was $25 \pm 3\%$ of its outer radius.

14. We detect no compact feature, which might be identified as a pulsar nebula, at or near the center of the shell at any epoch. At 8.4 GHz, we can place a limit of 0.11 mJy on the flux density of any such feature at $t = 2787$ d, and a limit of 0.05 mJy on average for the interval $2080 \text{ d} \leq t \leq 2787 \text{ d}$. These limits correspond to 0.7 and 0.3 times the current spectral luminosity of the Crab Nebula. We conclude either that any pulsar nebula in the center of SN 1993 is considerably less luminous than the Crab or that the interior of the shell cannot yet have become transparent by filamentation.

ACKNOWLEDGMENTS. We thank V. I. Altunin, A. J. Beasley, W. H. Cannon, J. E. Conway, D. A. Graham, D. L. Jones, A. Rius, G. Umana, and T. Venturi for help with several aspects of the project. J. Cadieux, M. Keleman, and B. Sorathia helped with some aspects of the VLBI data reduction during their tenure as students at York. We thank NRAO, the European VLBI Network, and the NASA/JPL Deep Space Network (DSN) for providing exceptional support for this extended and ongoing observing campaign. We also thank Natural Resources Canada for helping with the observations at the Algonquin Radio Observatory during the first years of the program. Research at York University was partly supported by NSERC. NRAO is operated under license by Associated Universities, Inc., under cooperative agreement with NSF. The European VLBI Network is a joint facility of European and Chinese radio astronomy institutes funded by their national research councils. The NASA/JPL DSN is operated by JPL/Caltech, under contract with NASA. We have made use of NASA's Astrophysics Data System Abstract Service.

REFERENCES

- Aldering, G., Humphreys, R. M., & Richmond, M. 1994, *AJ*, 107, 662
- Anderson, M. C., Jones, T. W., Rudnick, L., Tregilis, I. L., & Kang, H. 1994, *ApJ*, 421, L31
- Bandiera, R., Pacini, F., & Salvati, M. 1983, *A&A*, 126, 7
- Bandiera, R., Pacini, F., & Salvati, M. 1984, *ApJ*, 285, 134
- Bandiera, R., & van den Bergh, S. 1991, *ApJ*, 374, 186
- Bartel, N. et al. 1993, *IAU Circ.*, 5914
- Bartel, N., Bietenholz, M. F., & Rupen, M. P. 1995, *Proc. Nat. Acad. Sci.*, 92, 11374
- Bartel, N., et al. 1994, *Nature*, 368, 610
- Bartel, N., et al. 2000, *Science*, 287, 112
- Bartel, N., et al. 2002, *ApJ*, 581, 404 (Paper II)
- Bartunov, O. S., Blinnikov, S. I., Pavlyuk, N. N., & Tsetkov, D. Yu. 1994, *A&A*, 281, L53
- Bietenholz, M. F., Bartel, N., & Rupen, M. P. 2000, *ApJ*, 532, 895
- Bietenholz, M. F., Bartel, N., & Rupen, M. P. 2001, *ApJ*, 557, 770 (Paper I)
- Bietenholz, M. F., et al. 2001, *IAU Symp. 205: Galaxies and Their Constituents at the Highest Angular Resolutions*, eds. R. A. Schilizzi, S. N. Vogel, F. Paresce and M. S. Elvis, (San Francisco: ASP), 380
- Blondin, J. M., Lundqvist, P., & Chevalier, R. A. 1996, *ApJ* 472, 257
- Briggs, D. S. 1995, *High Fidelity Deconvolution of Moderately Resolved Sources*, (PhD Thesis), NRAO
- Briggs, D. S., Schwab, F. R., & Sramek, R. A. 1998, in *Synthesis Imaging in Radio Astronomy II*, ASP Conference Series, vol. 180, ed. G. B. Taylor, C. L. Carilli, & R. A. Perley (San Francisco: ASP), 127
- Braun, R., Gull, S. F., & Perley, R. A. 1987, *Nature*, 327, 395
- Brunthaler, A., Bower, C. G., Falcke, H., & Mellon, R. R., 2001, *ApJ*, 560L, 123
- Burrows, A., Hayes, J., & Fryxell, B. A. 1995, *ApJ*, 450, 830
- Chevalier, R. A. 1982a, *ApJ*, 258, 790
- Chevalier, R. A. 1982b, *ApJ*, 259, 85
- Chevalier, R. A. 1982c, *ApJ*, 259, 302
- Chevalier, R. A. 1998, *ApJ*, 499, 810
- Chevalier, R. A., Blondin, J. M., & Emmering, R. T. 1992, *ApJ*, 392, 118
- Chevalier, R. A., & Fransson, C. 1992, *ApJ*, 395, 540
- Cid-Fernandes, R., Plewa, T., Różycka, M., Franco, J., Terlevich, R., Tenorio-Tagle, G., & Miller, W. 1996, *MNRAS*, 283, 419
- Clocchiatti, A., Wheeler, J. C., Barker, E. S., Filippenko, A. V., Matheson, T., & Liebert, J. W. 1995, *ApJ*, 446, 167
- Cornwell, T. J. 1988, *A&A*, 202, 316
- Cornwell, T. J., & Braun, R. 1999, in *ASP Conference Series vol. 180, Synthesis Imaging in Radio Astronomy II*, ed. G. B. Taylor, C. L. Carilli & R. A. Perley, (San Francisco: ASP), 151
- Dickel, J. R., van Breugel, W. J. M., & Strom, R. G. 1991, *AJ*, 101, 2151
- Ferrarese, L., et al. 2000, *ApJS*, 128, 431
- Filippenko, A. V., Matheson, T., & Barth, A. J. 1994, *AJ*, 108, 2220
- Fransson, C. & Björnsson, C.-I. 1998, *ApJ*, 509, 861
- Freedman, W. L., et al. 1994, *ApJ*, 427, 628
- Freedman, W. L., et al. 2001, *ApJ*, 553, 47
- Fryxell, B. 1994, in *Numerical Simulations in Astrophysics*, (Cambridge: Cambridge University Press), 149
- Gull, S. F. 1973, *MNRAS*, 161, 47
- Höflich, P. 1995, *ApJ*, 440, 821
- Höflich, P., Wheeler, J. C., Hines, D. C., & Trammell, S. R., 1996, *ApJ*, 459, 307
- Höflich, P., Langer, N., & Duschinger, M. 1993, *A&A*, 275, L29
- Houck J. C., & Fransson, C. 1996, *ApJ*, 456, 811
- Humphreys, R. M., Aldering, G. S., Bryja, C. O., & Thurmes, P. M. 1993, *IAU Circ.* 5739
- Jones, T. W., Rudnick, L., Jun, B.-I., Borkowski, K. J., Dubner, G., Frail, D. A., Kang, H., Kassim, N. E., & McCray, R. 1998, *PASP*, 110, 125
- Jun, B.-I. 1998, *ApJ*, 499, 282
- Jun, B.-I., & Norman, M. L. 1996a, *ApJ*, 465, 800
- Jun, B.-I., & Norman, M. L. 1996b, *ApJ*, 472, 245
- Jun, B.-I., & Jones, T. W. 1999, *ApJ*, 511, 774
- Jun, B.-I., Jones, T. W., & Norman, M. L. 1996, *ApJ*, 468, L59
- Lewis, J. M., et al. 1994, *MNRAS*, 266, L29
- Linfield, R. P. 1986, *AJ*, 92, 213
- Marcaide, J. M., et al. 1993, *IAU Circ.*, 5785
- Marcaide, J. M., et al. 1994, *ApJ*, 424, L25
- Marcaide, J. M., et al. 1995a, *Nature*, 373, 44
- Marcaide, J. M., et al. 1995b, *Science*, 270, 1475
- Marcaide, J. M., et al. 1997, *ApJ*, 486, L31
- Marcaide, J. M., et al. 2002 in *Proceedings of the European VLBI Network Symposium*, eds. E. Ros, R. W. Porcas, A. P. Lobanov & J. A. Zensus, 239
- Massi, M., & Aaron, S. 1999, *A&ASuppl.* 136, 211
- Mioduszewski, A. J., Dwarkadas, V. V., & Ball, L. 2001, *ApJ*, 562, 869
- Milne, D. K. 1987, *Australian J. Phys.*, 771
- Monnier, J. D., Tuthill, P. G., Lopez, B., Cruzalebes, P., Danchi, W. C., & Haniiff, C. A. 1999, *ApJ*, 512, 351
- Müller, E., Fryxell, B., & Arnett, D. 1991, *A&A*, 251, 505
- Nomoto, K., Suzuki, T., Shigeyama, T., Kumagai, S., Yamaoka, H., & Saio, H. 1993, *Nature*, 364, 507
- Pacholczyk, A.G. 1970, *Radio Astrophysics* (San Francisco: Freeman)
- Perley, R. A. 1999, in *ASP Conf. Proc. 180, Synthesis Imaging in Radio Astronomy II*, eds. G. B. Taylor, C. L. Carilli, & R. A. Perley (San Francisco: ASP), 275
- Podsiadlowski, Ph., Hsu, J. J. L., Joss, P. C., & Ross, R. R. 1993, *Nature*, 364, 509
- Reynolds, S. P. 1985, *ApJ*, 278, 630
- Reynolds, S. P., & Chevalier, R. A. 1984, *ApJ*, 278, 630
- Ripero, J., & Garcia, F. 1993, *IAU Circ.*, 5731
- Rohlfs, K. & Wilson, T. L. 1996, *Tools of Radio Astronomy* (Berlin: Springer).
- Seward, F., Gorenstein, P., & Tucker, W. 1983, *ApJ*, 266, 287
- Shigeyama, T., Suzuki, T., Kumagai, S., Nomoto, K., Saio, H., & Yamaoka, H. 1994, *ApJ*, 420, 341
- Spyromilio, J. 1994, *MNRAS*, 266, L61
- Trammell, S. R., Hines, D. C., & Wheeler, J. C. 1993, *ApJ*, 414, L21
- Tran, H. D., Filippenko, A. V., Schmidt, G. D., Bjorkman, K. S., Jannuzi, B. T., & Smith, P. S. 1997, *PASP*, 109, 489
- Van Dyk, S. D., Weiler, K. W., Sramek, R. A., Rupen, M. P. & Panagia, N. 1994, *ApJ*, 432, L115
- Van Dyk, S. D., Garnavich, P. M., Filippenko, A. V., Höflich, P., Kirshner, R. P., Kurucz, R. L., & Challis, P. 2002, *PASP*, 114, 1322
- Walker, R. C. 1999 in *ASP Conf. Proc. 180, Synthesis Imaging in Radio Astronomy II*, ed. G. B. Taylor, C. L. Carilli, & R. A. Perley (San Francisco: ASP), 433
- Wang, L., & Hu, J. 1994, *Nature*, 369, 380
- Wardle, J. F. C., & Kronberg, P. P. 1974, *ApJ*, 194, 249
- Weiler, K. W., Panagia, N., Montes, M. J., & Sramek, R. A. 2002, *ARA&A*, 40, 387
- Wheeler, J. C., et al. 1993, *ApJ*, 417, L71
- Woosley, S. E., Eastman, R. G., Weaver, T. A., & Pinto, P. A. 1994, *ApJ*, 429, 300

TABLE 1
PARAMETERS OF THE SN 1993J IMAGES AT 8.4 AND 5 GHz

Date	Age ^a	Resolution ^b	8.4 GHz Peak brightness (mJy beam ⁻¹)	σ_{bg} ^c (mJy beam ⁻¹)	Resolution ^b	5.0 GHz Peak brightness (mJy beam ⁻¹)	σ_{bg} ^c (mJy beam ⁻¹)
	(days)	(mas)			(mas)		
1993 May 17	50	0.45 ^d	45.5	0.30			
1993 Jun 27	91	0.46 ^d	83.3	0.36			
1993 Sep 19	175	0.47 ^e	23.3	0.27	0.80 ^d	61.7	1.28
1993 Nov 6	223	0.49	15.6	0.11			
1993 Dec 17	264	0.50	12.1	0.10			
1994 Jan 28	306	0.54	9.83	0.24			
1994 Mar 15	352	0.57	6.23	0.15	0.85	19.80	0.17
1994 Apr 22	390	0.60	6.25	0.13	0.88 ^e	18.75	0.30
1994 Jun 22	451	0.69	6.32	0.073	0.90 ^d	13.57	0.21
1994 Aug 30	520	0.73	4.81	0.14	0.95	10.84	0.10
1994 Oct 31	582	0.74	4.73	0.14	1.00 ^d	10.45	0.23
1994 Dec 23	635	0.78	4.17	0.10	1.01	8.79	0.14
1995 Feb 12	686	0.80	3.66	0.061			
1995 May 11	774	1.00	4.66	0.25			
1995 Aug 18	873				1.03	3.87	0.084
1995 Dec 19	996	0.93	1.90	0.088	1.04 ^d	3.86	0.20
1996 Apr 8	1107	0.97	1.60	0.087	1.05 ^e	2.91	0.11
1996 Sep 1	1253	1.02	1.62	0.065	1.05	2.28	0.040
1996 Dec 13	1356	1.05	2.59	0.056	1.05	1.81	0.034
1997 Jun 7	1532	1.10	1.20	0.064			
1997 Nov 15	1693	1.12	1.00	0.042	1.12	1.12	0.034
1998 Jun 3	1893 ^f	1.12	0.91	0.029	1.12	1.20	0.031
1998 Nov 20	2064				1.12	0.97	0.021
1998 Dec 7	2080	1.12	0.88	0.038			
1999 Jun 16	2271				1.12	0.84	0.040
1999 Nov 23	2432				1.12	0.71	0.037
2000 Feb 25	2525	1.12	0.48	0.040			
2000 Nov 13	2787	1.12	0.32	0.030			
2001 Jun 10	2996				1.12	0.42	0.016
2002 May 25	3345				1.12	0.34	0.019

^aTime in days since shock breakout on 28.0 March 1993.

^bEffective angular resolution, i.e., FWHM of the circular Gaussian convolving beam.

^cStandard deviation of the background brightness, see text §3.2.

^dSuper-resolved, by less than 50%.

^eSuper-resolved along the long axis of the beam only, CLEAN beam preserves area of the dirty beam.

^fThe 5.0 GHz observations actually occurred 1 day earlier.

TABLE 2
PERCENTAGE LINEAR POLARIZATION OF SN 1993J

Date	t^a	Frequency	Resolution ^b	Mean Polarization for $I > 60\%$ of peak ^{c,d}		Polarization of Image Peak ^d	
	(d)	(GHz)	(mas)	value (%)	3σ upper limit (%)	value (%)	3σ upper limit (%)
1995 Aug 17	873	5.0	0.93	0.2 ± 0.7	2.3	$+0.5 \pm 1.7$	6
1996 Dec 13	1356	8.4	1.29	1.1 ± 1.1	4.4	$+2.9 \pm 2.1$	9
1998 Nov 20	2064	5.0	0.96	1.2 ± 0.9	3.9	-2.1 ± 2.4	5
2001 Nov 26	3164	1.7	2.61	0.5 ± 0.7	2.6	-0.8 ± 1.7	4

^aThe number of days since shock breakout on 28 March 1993.

^bThe angular resolution (geometric mean of the FWHM of the major and minor axes of the Gaussian restoring beam). The weighting used in imaging was chosen to maximize the signal-to-noise ratio, therefore the beam size may differ from the corresponding one in Table 1 and Figure 2.

^cThe (scalar) mean percentage linear polarization over the region where the brightness in Stokes I is $> 60\%$ of the image peak.

^dAll percentage polarizations are corrected for the noise bias. They are therefore correct on average, but sometimes unphysically negative; see text §3.6.

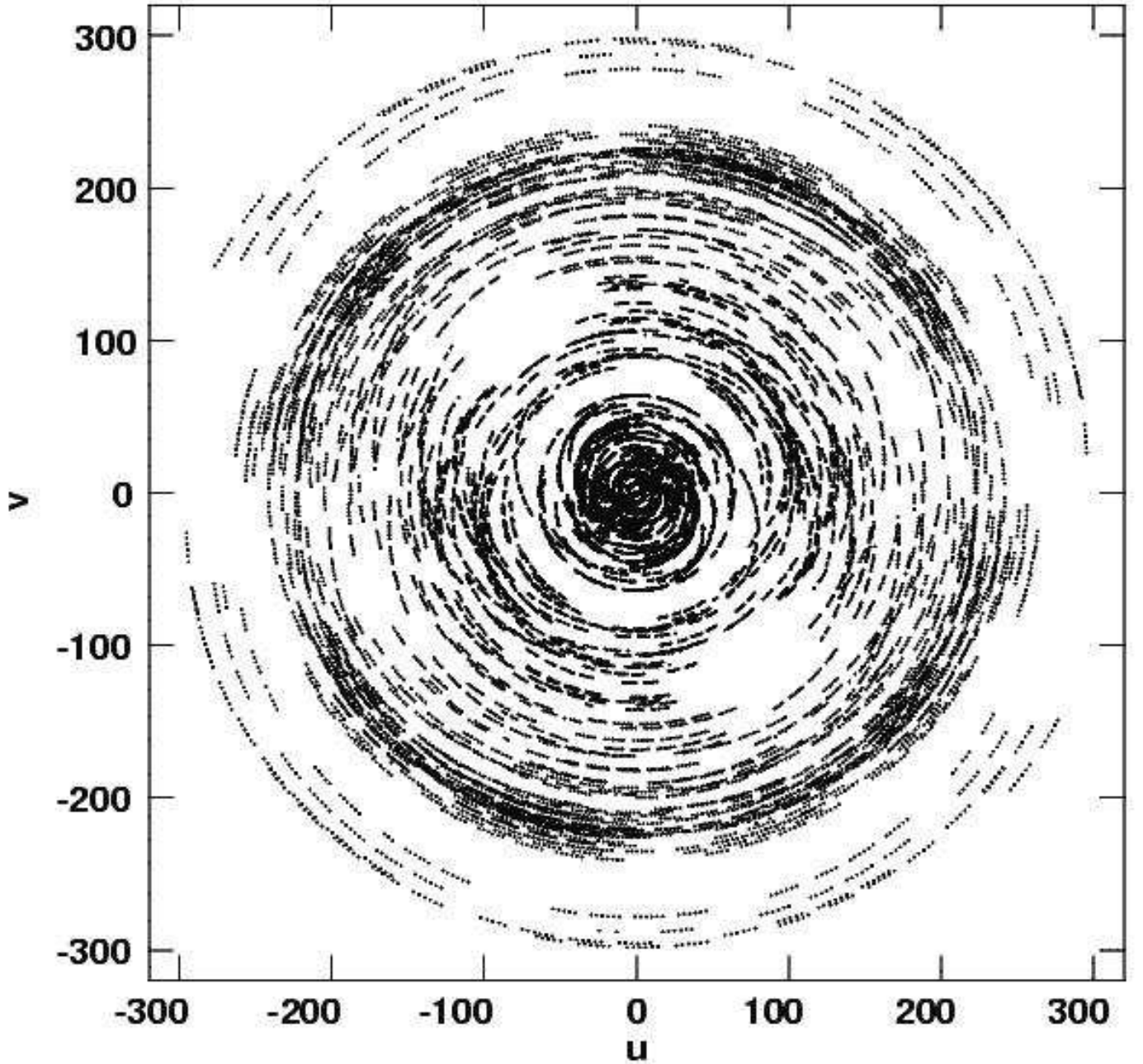
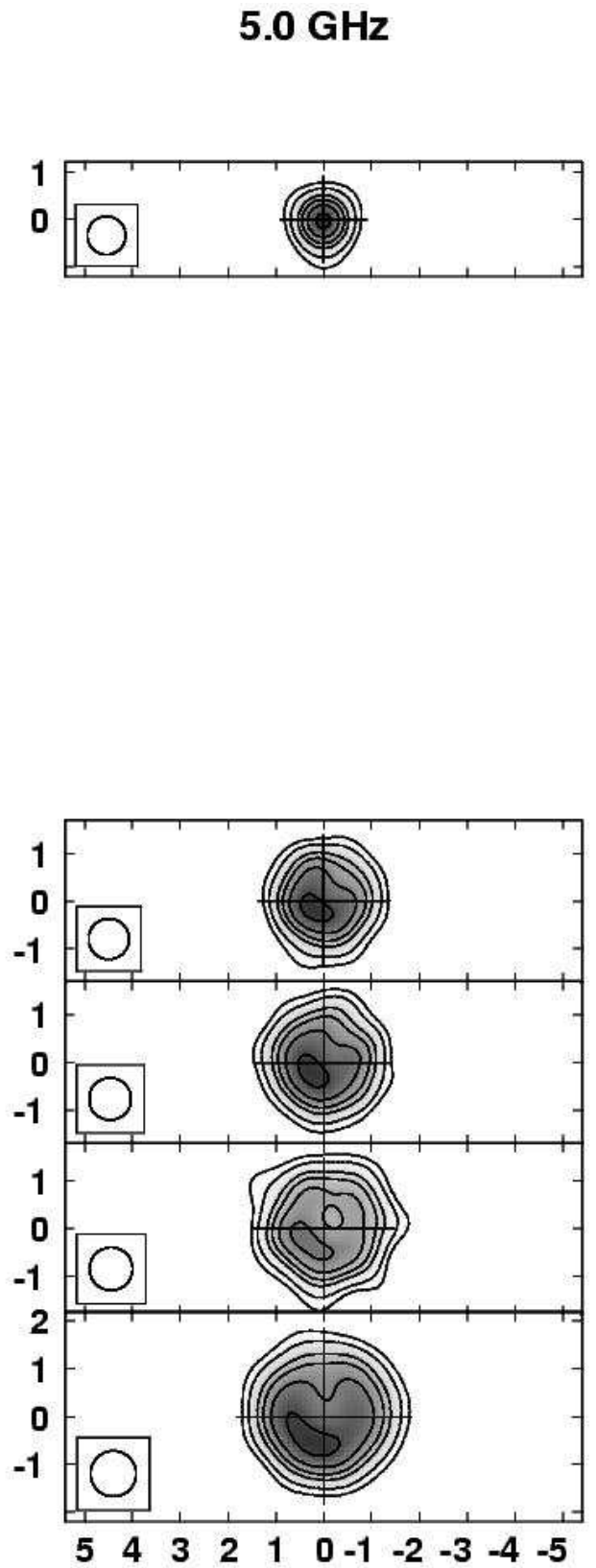
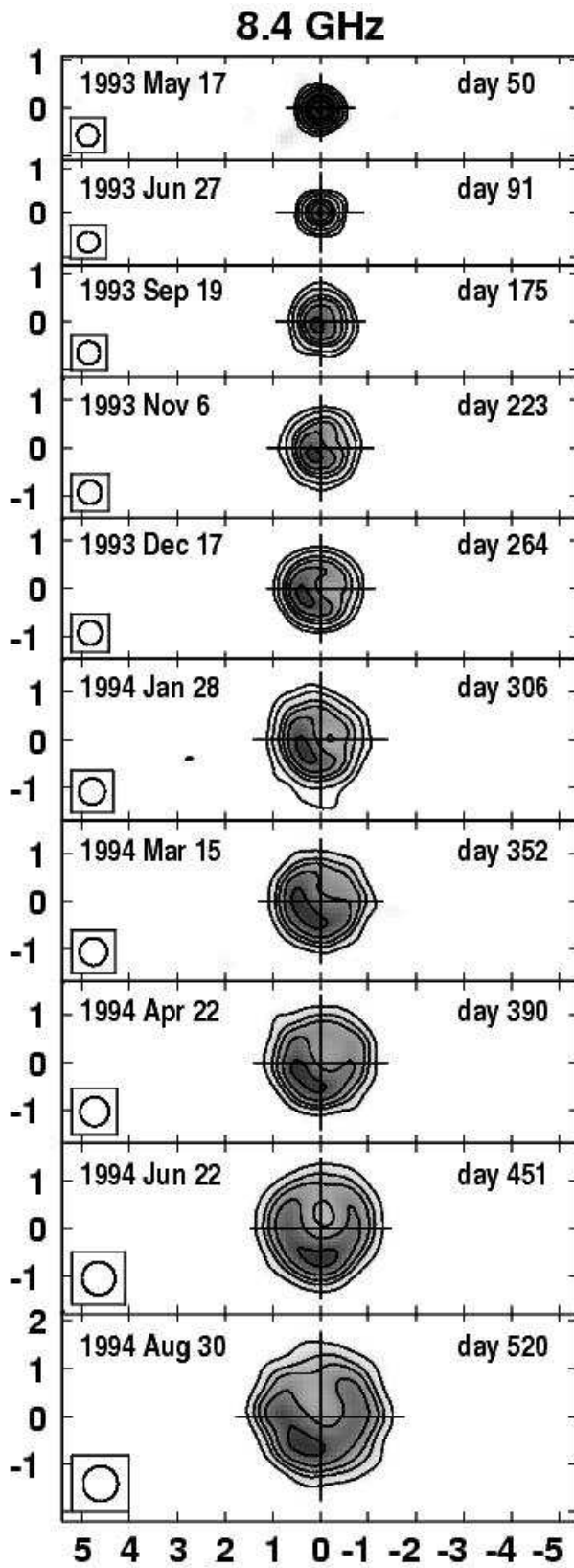
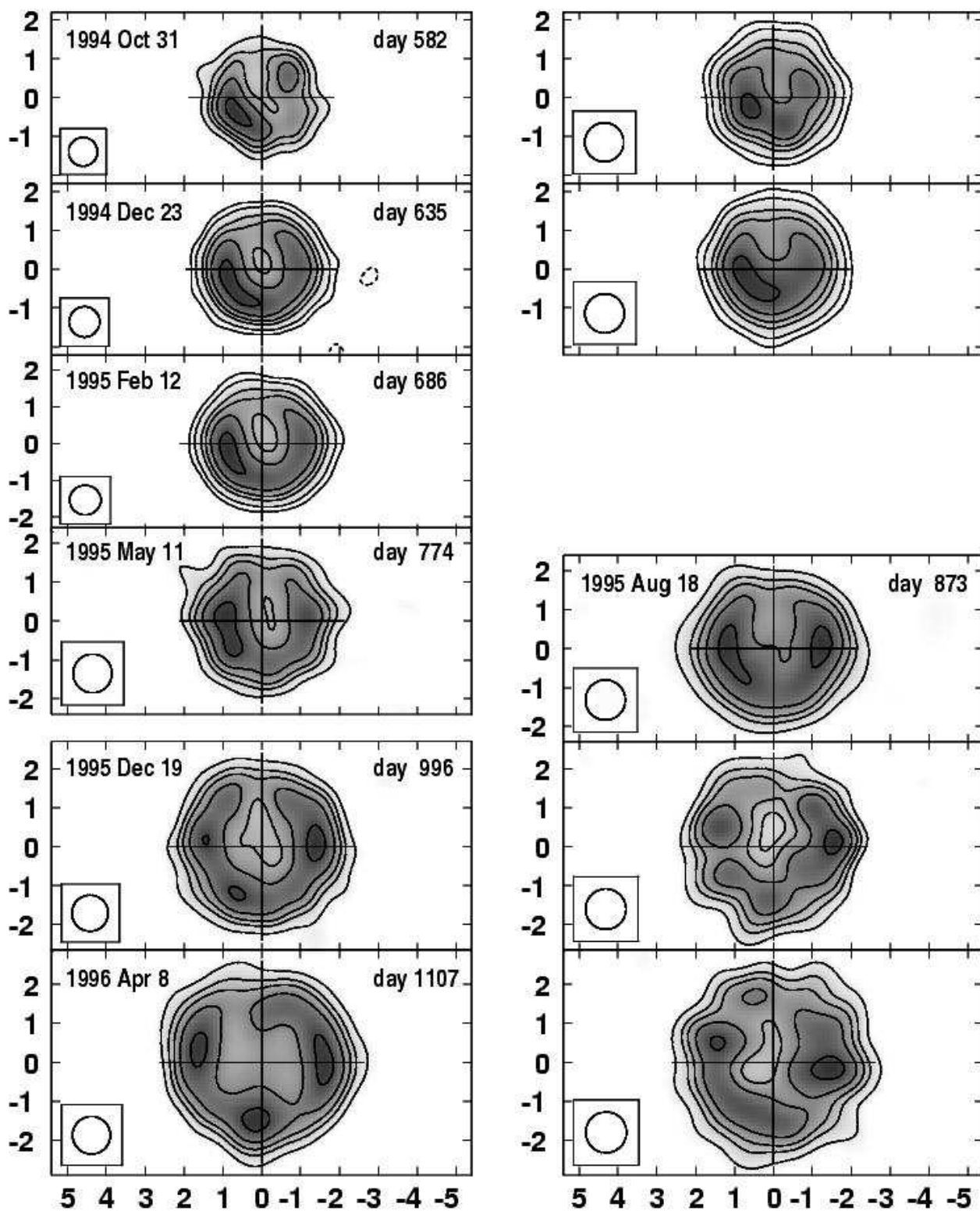
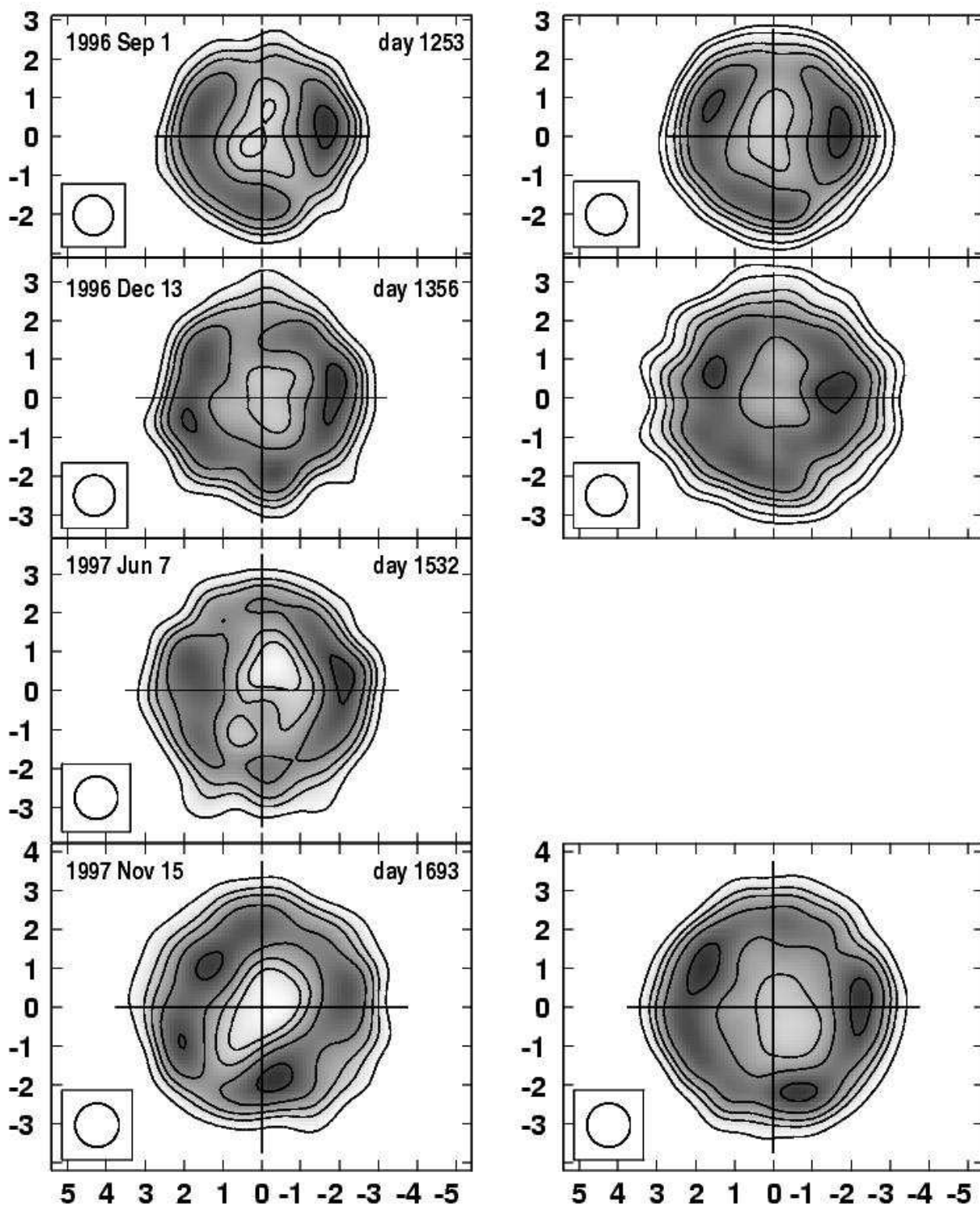
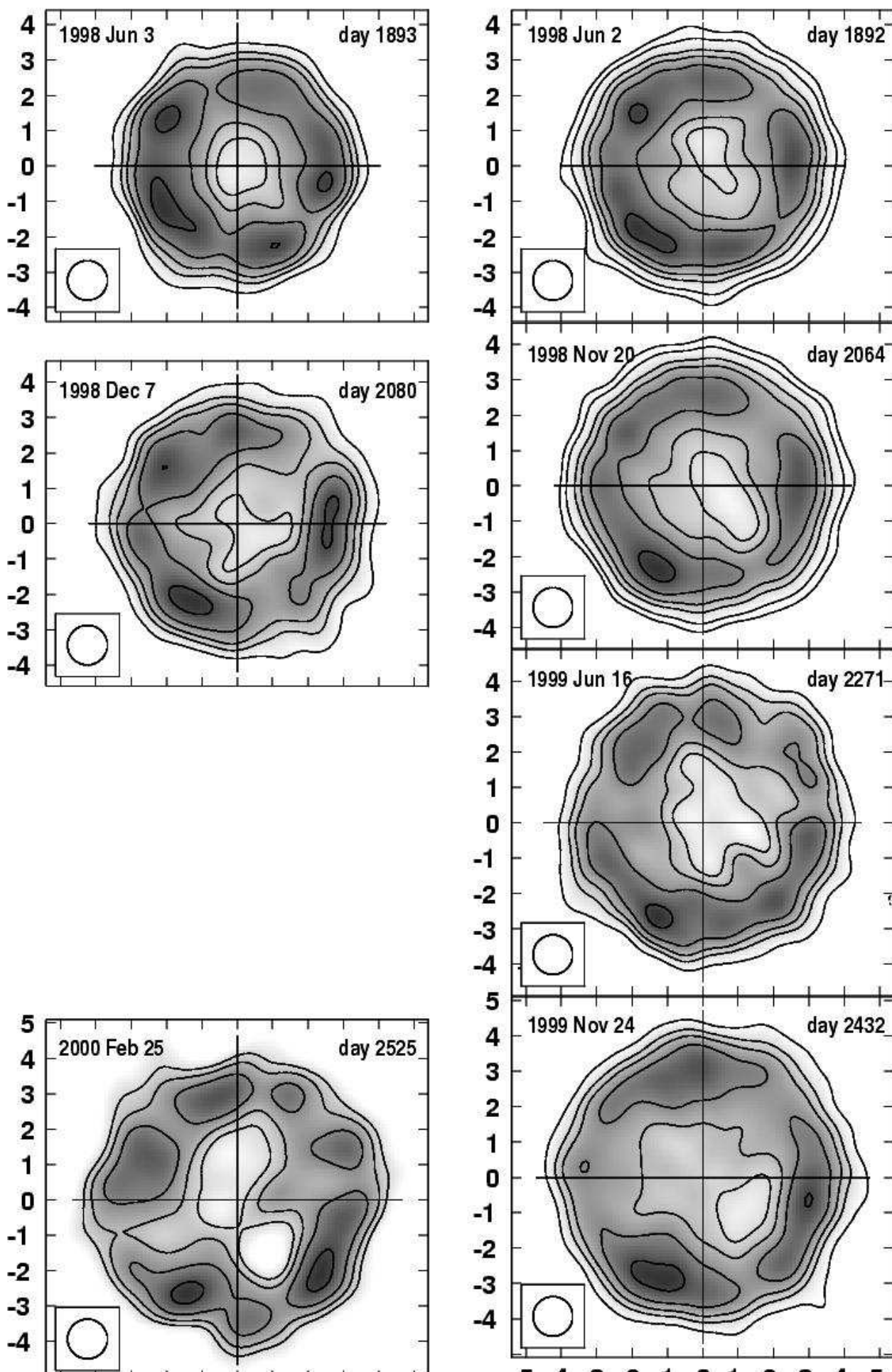


FIG. 1.— The u - v coverage of our observations at $t = 2787$ d (2000 November 13) at 8.4 GHz, showing the dense and nearly circular u - v coverage. Both u and v are given in Mega-wavelengths.









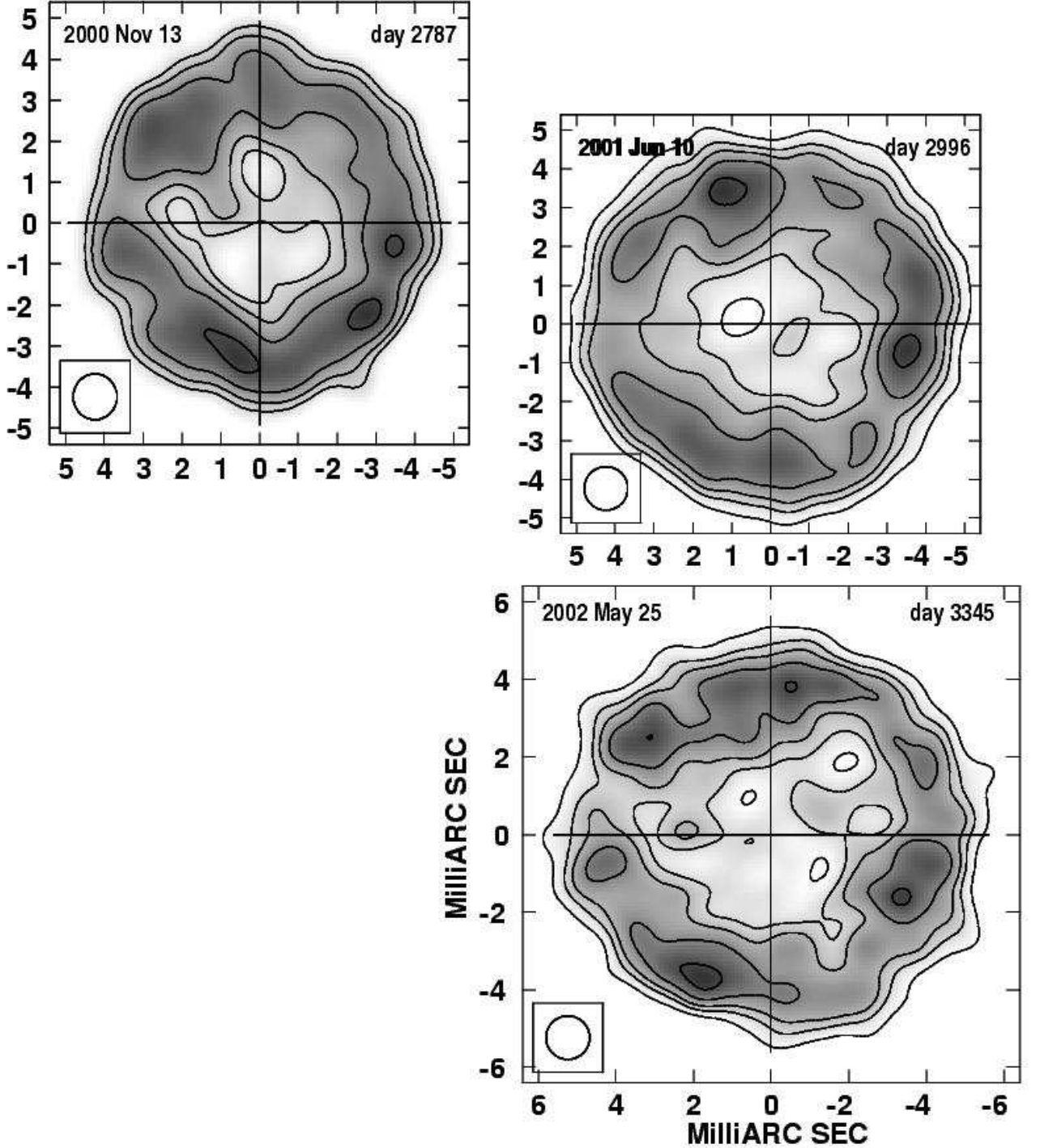
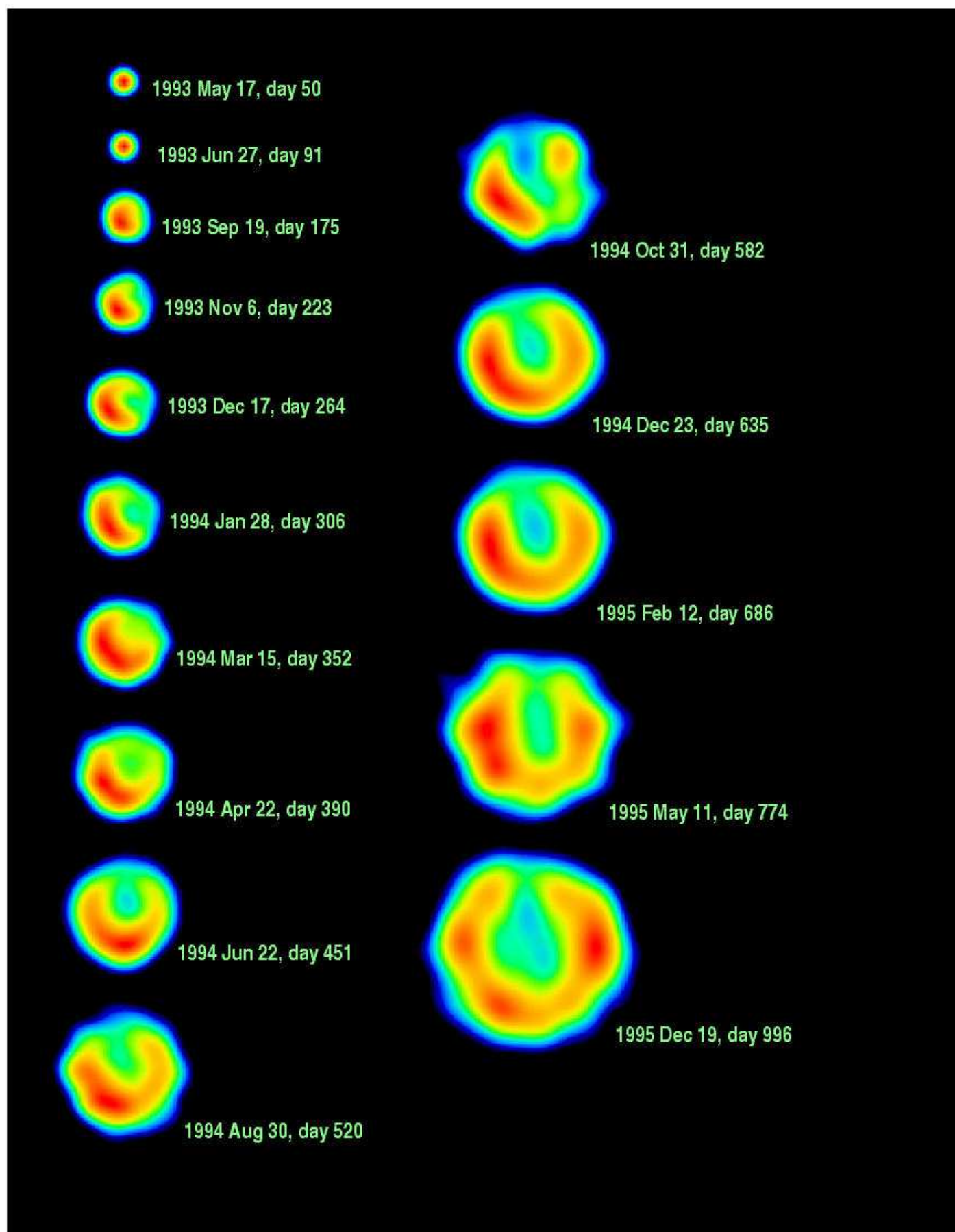
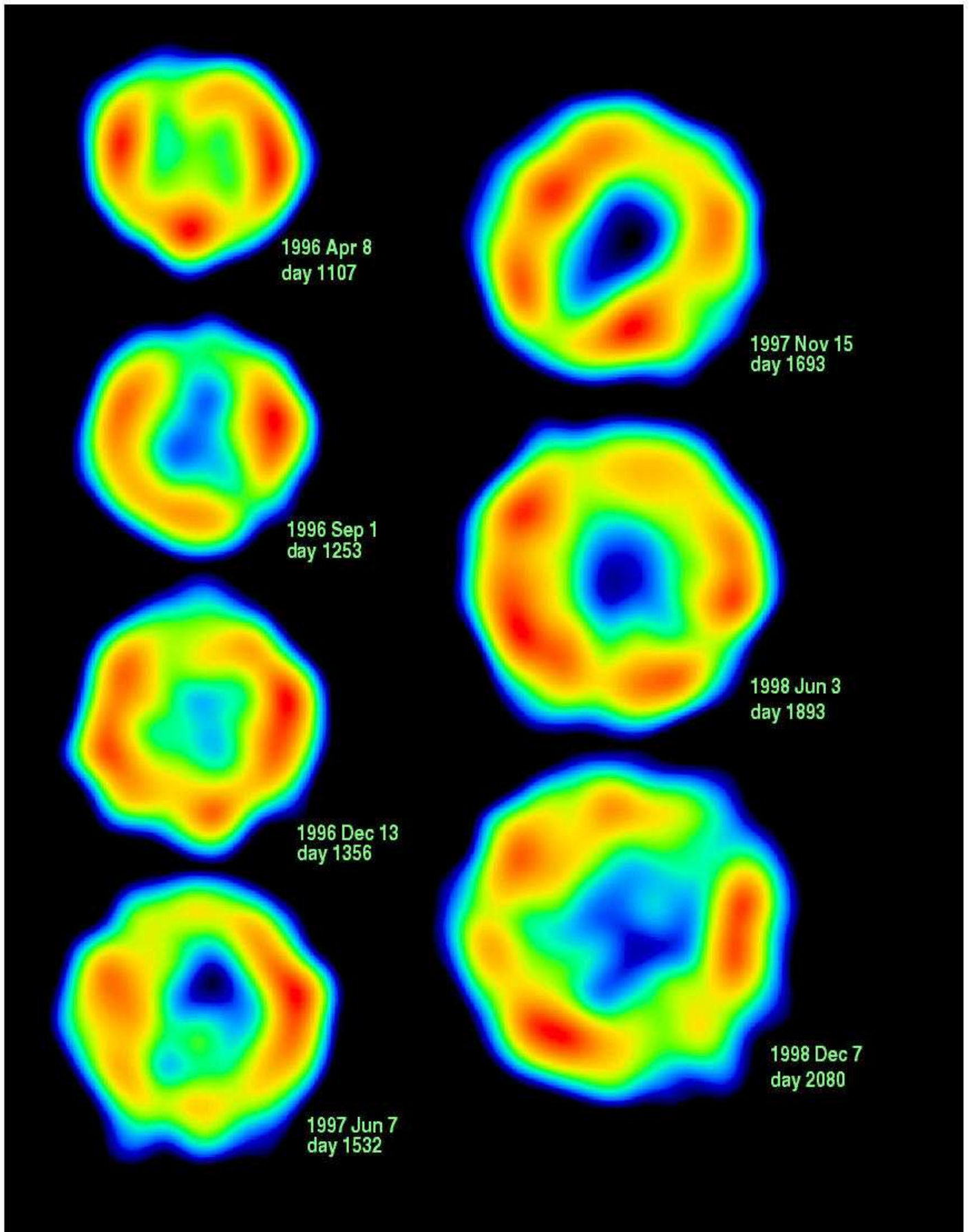


FIG. 2.— VLBI images of SN 1993J at 8.4 GHz, in the left column, and at 5.0 GHz, in the right column. The resolution is shown at the lower left in each panel. The greyscale runs from 8 to 100% of the peak brightness for images for $t \leq 1253$ d, and from 16 to 100% of the peak brightness thereafter. The contours are drawn at 1, 2, 4, ..., 32, 45, 64 and 90% of the peak brightness, starting at the first contour greater than $3 \sigma_{bg}$, where σ_{bg} is the standard deviation of the background brightness. See Table 1 for σ_{bg} , the peak brightness, and the FWHM of the convolving beam. At most epochs, we switched between 8.4 and 5 GHz during the observing run, and the images at each frequency are presented side by side with the date and day number indicated only in the 8.4 GHz panel. For the remaining epochs, there were separate observing runs for 8.4 and 5 GHz, and these cases are represented by offset image panels. (See Fig. 3 for a false-color version of the 8.4 GHz images). On this and on all our subsequent images, north is up and east to the left, and the origin of the coordinate system, indicated by the large crosses, is at the center of the fitted supernova shell. On average, the fitted centers are within $64 \mu\text{s}$ rms of the explosion center at 8.4 GHz. See Paper I for the offsets of the fitted center and explosion center for the individual images.





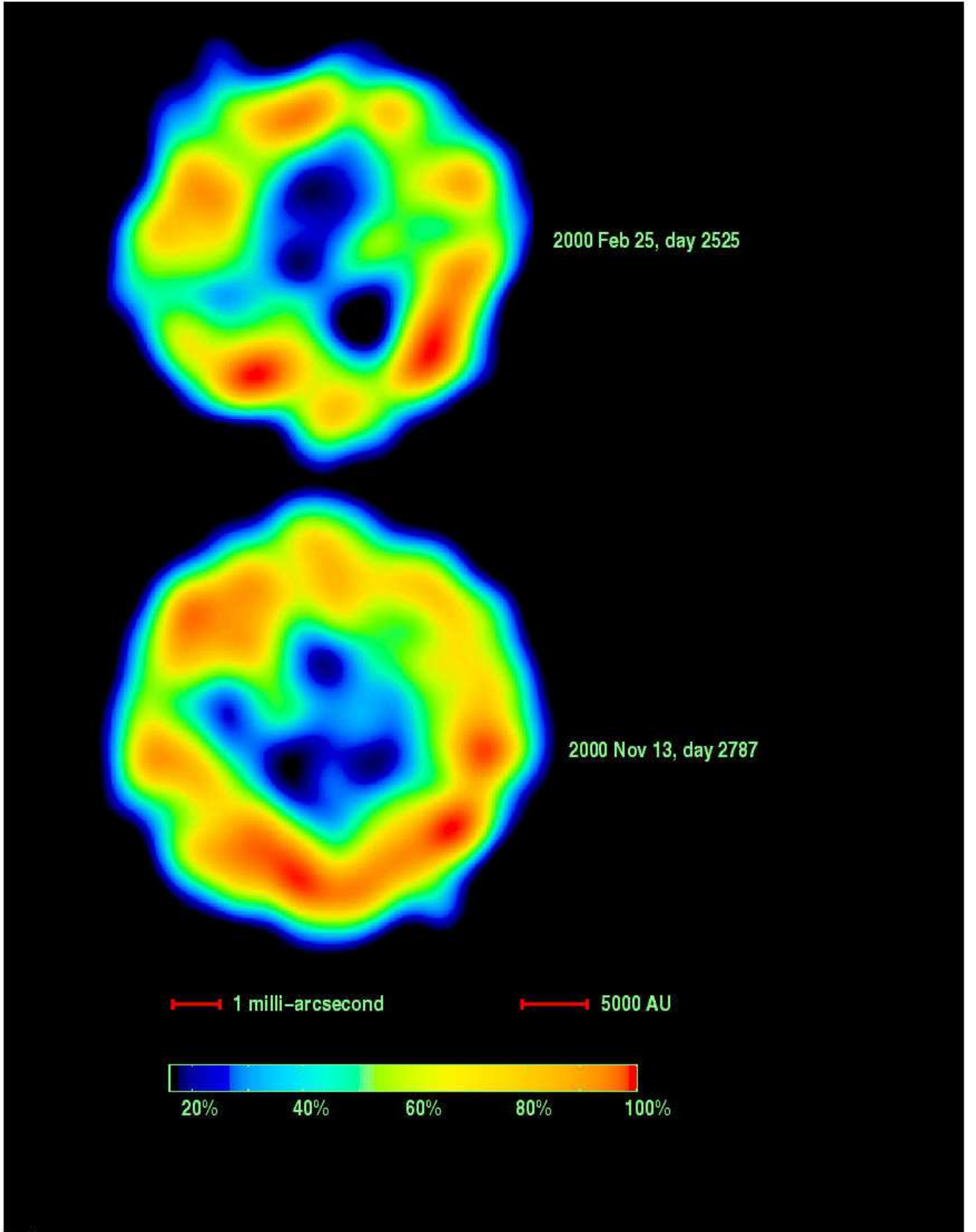


FIG. 3.— The VLBI images of SN 1993 at 8.4 GHz in false colour. The brightness scale, indicated at the end, runs from 16 to 100% of the peak brightness in each image. Table 1 lists the peak brightness and the FWHM of the convolving beam for each image.

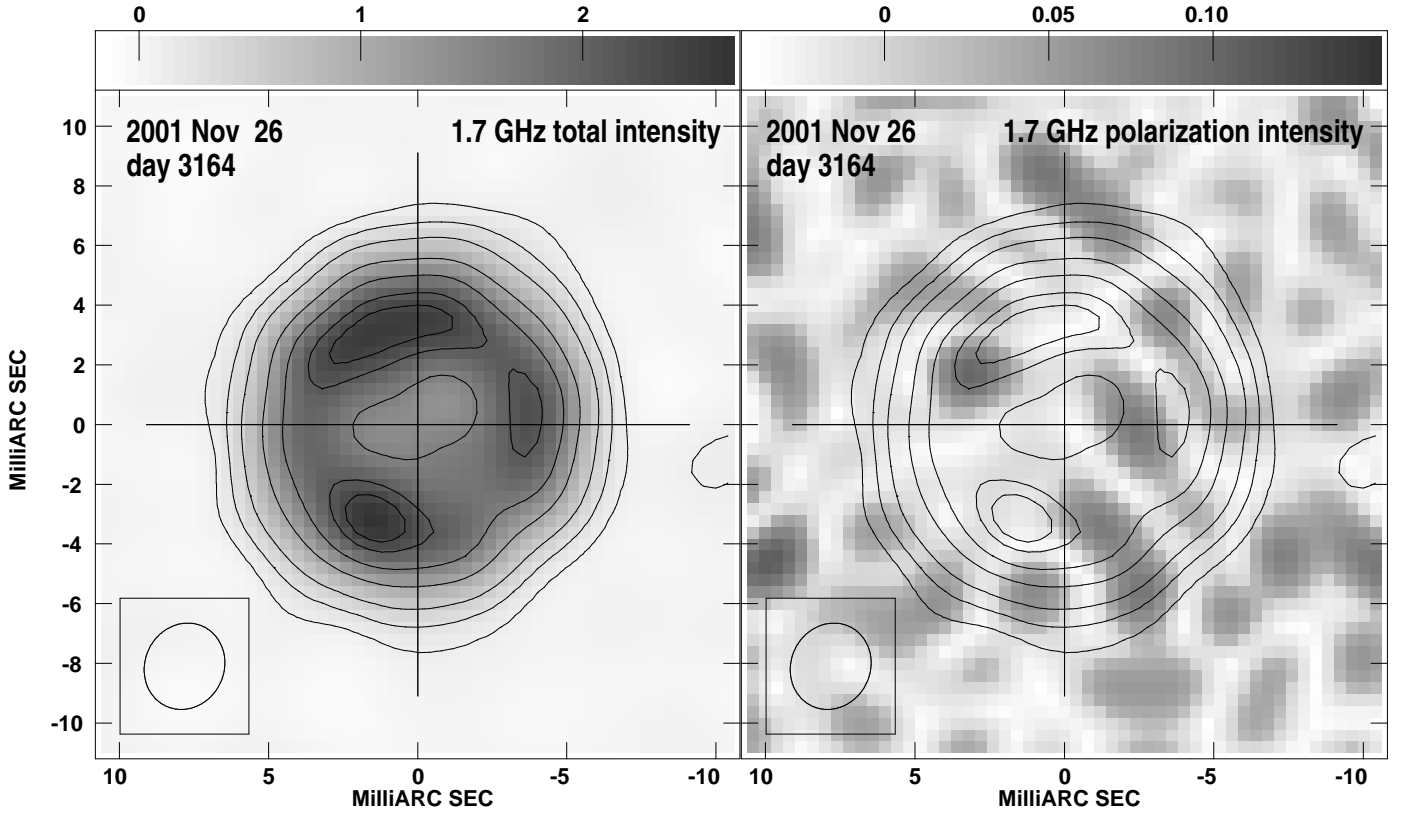


FIG. 4.— Our latest 1.7 GHz VLBI image of SN 1993J, observed at $t = 3164$ d. The resolution is shown at the lower left and the greyscales are labeled in mJy beam^{-1} in both panels. At left, we show the total intensity (Stokes I), with contours drawn at $-3.6, 3.6, 10, 20, 40, 60, 80$, and 90% of the peak brightness of $2.66 \text{ mJy beam}^{-1}$. The rms background brightness, σ_{bg} , was $32 \mu\text{Jy beam}^{-1}$. At right, we show the linear polarization intensity ($S_{\text{pol}} = \sqrt{Q^2 + U^2}$), corrected for the noise bias, and hence being sometimes unphysically negative. The total intensity contours are repeated for reference.

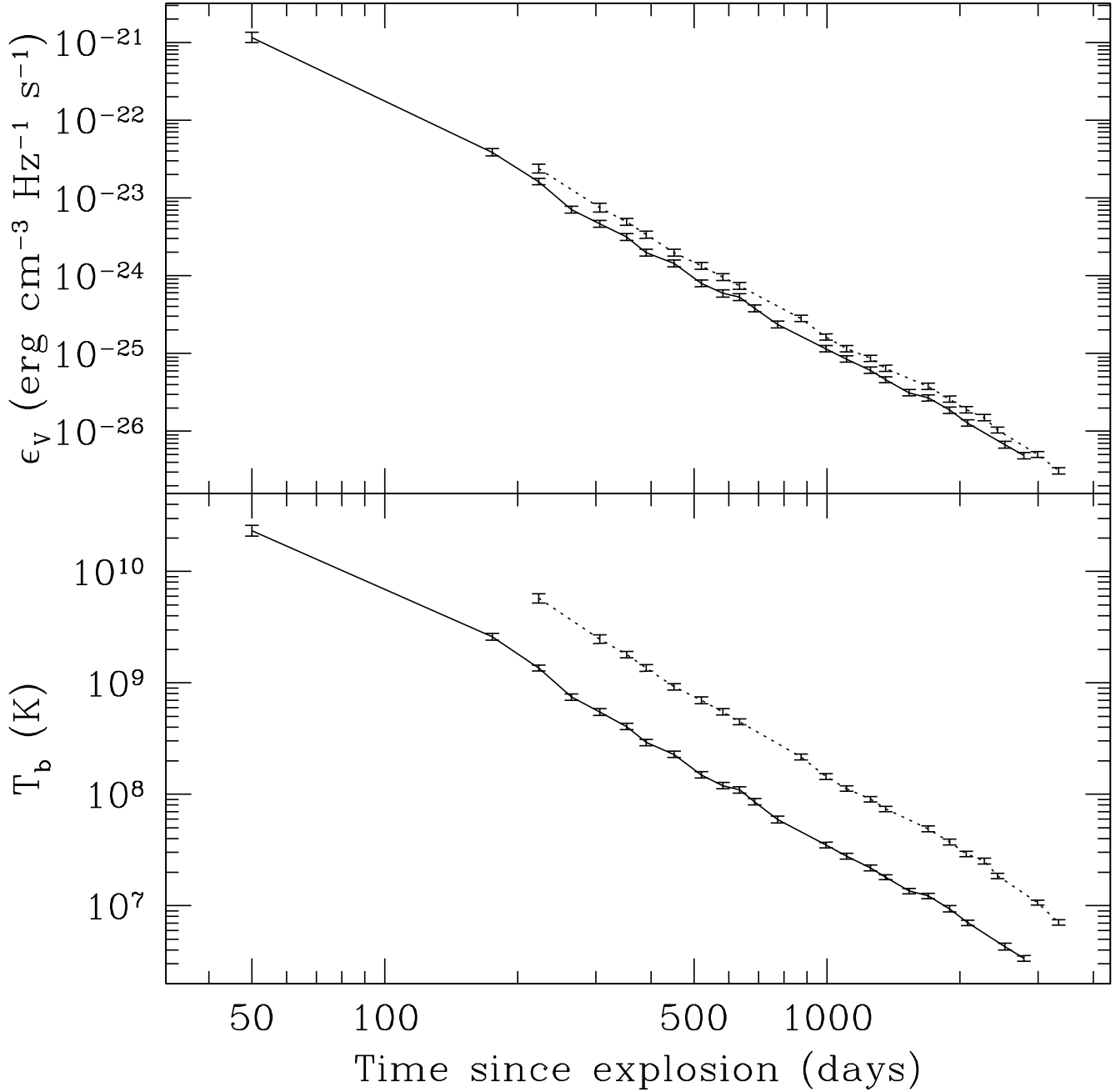


FIG. 5.— The mean spectral volume emissivity, ϵ_v , and brightness temperature, T_b , of SN 1993J as a function of time at 8.4 and 5.0 GHz. We calculate ϵ_v and T_b from the total flux densities measured at the VLA by taking the outer angular radius of SN 1993J to be the fit value of θ_o (see Paper II). For ϵ_v , we take a distance of 3.6 Mpc. We also assume a spherical shell with a ratio of the outer to the inner radius of 1.34 and without any absorption. The uncertainties are approximately standard errors.

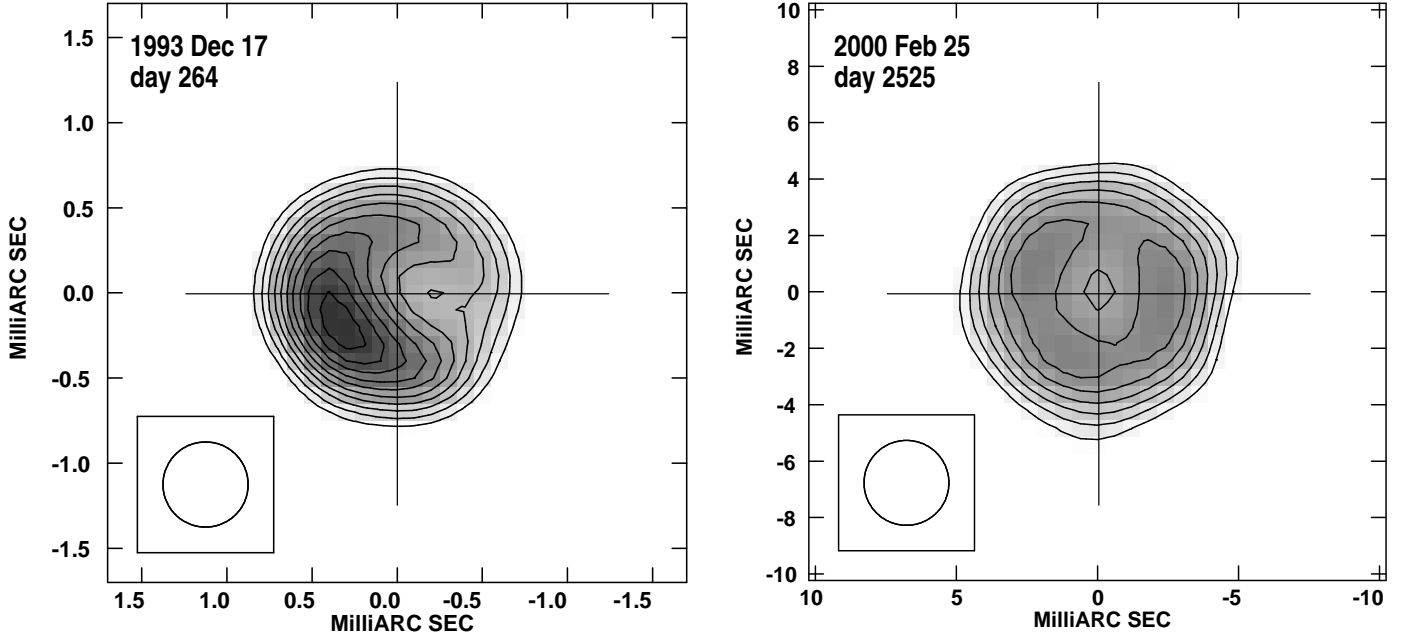


FIG. 6.— A comparison of two 8.4-GHz images of SN 1993J convolved to the same resolution relative to the outer angular radius of the fit shell. Left: the image from $t = 264$ d, convolved to 0.5 mas resolution. Right: the image from $t = 2525$ d, convolved to 3.0 mas resolution. The contours are comparable in both images and are drawn at 6, 8, 10, ... 24% of the total flux density per beam area. The greyscale is labeled in mJy beam^{-1} and runs from 5 to 25% of the total flux density per beam area.

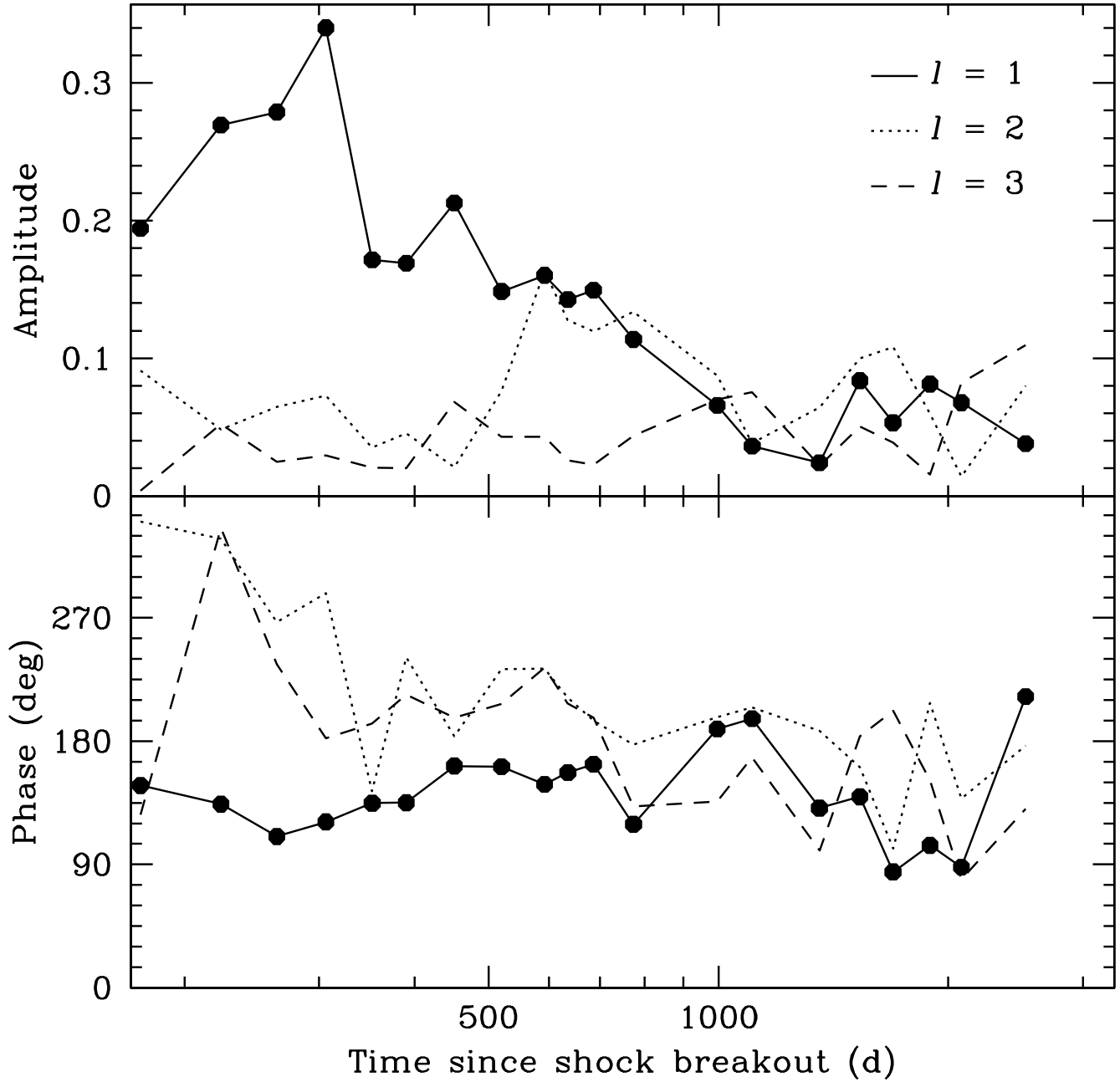


FIG. 7.— The amplitudes and phases of the first three harmonics ($l = 1, 2, 3$) of the Fourier expansion of the modulation of the brightness of the radio shell at 8.4 GHz as a function of position angle, p.a., (integrated in radius). The wave number, l , is the number of maxima along the circumference. For $l = 1$, the phase is the p.a. of the maximum. For $l > 1$, the phase is the p.a. of the first maximum multiplied by l .

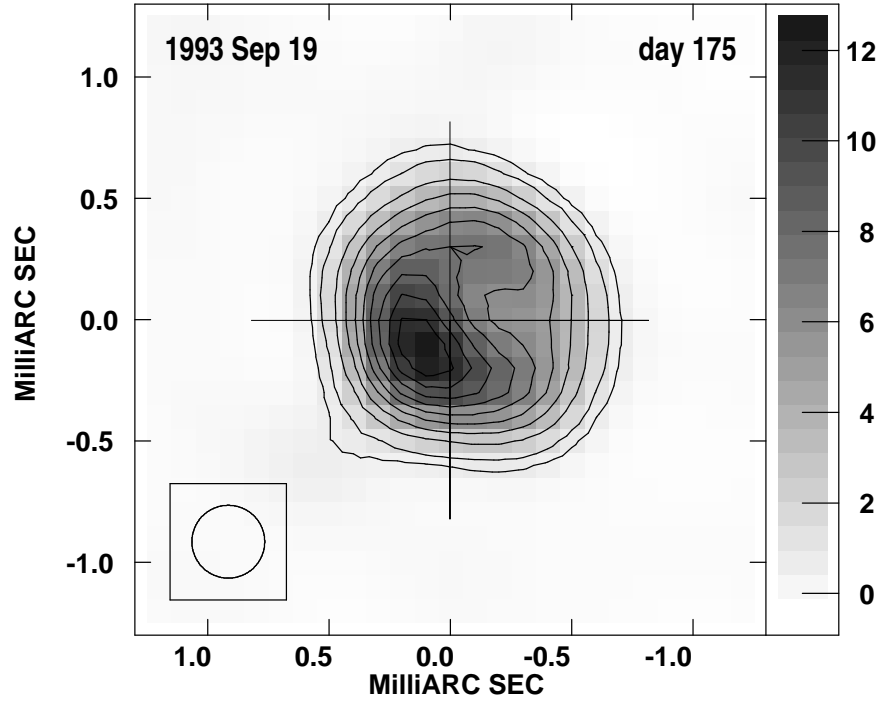


FIG. 8.— A high-resolution image of SN 1993J at 8.4 GHz at $t = 175$ d. The resolution was 0.3 mas and is shown in the lower left. The greyscale at right is labeled in mJy beam^{-1} . The contours are drawn at $-5, 5, 10, 20, 30, 40, 50, 60, 70, 80$, and 90% of the peak brightness of $12.5 \text{ mJy beam}^{-1}$. Maximum entropy deconvolution was used, and σ_{bg} was $78 \mu\text{Jy beam}^{-1}$.

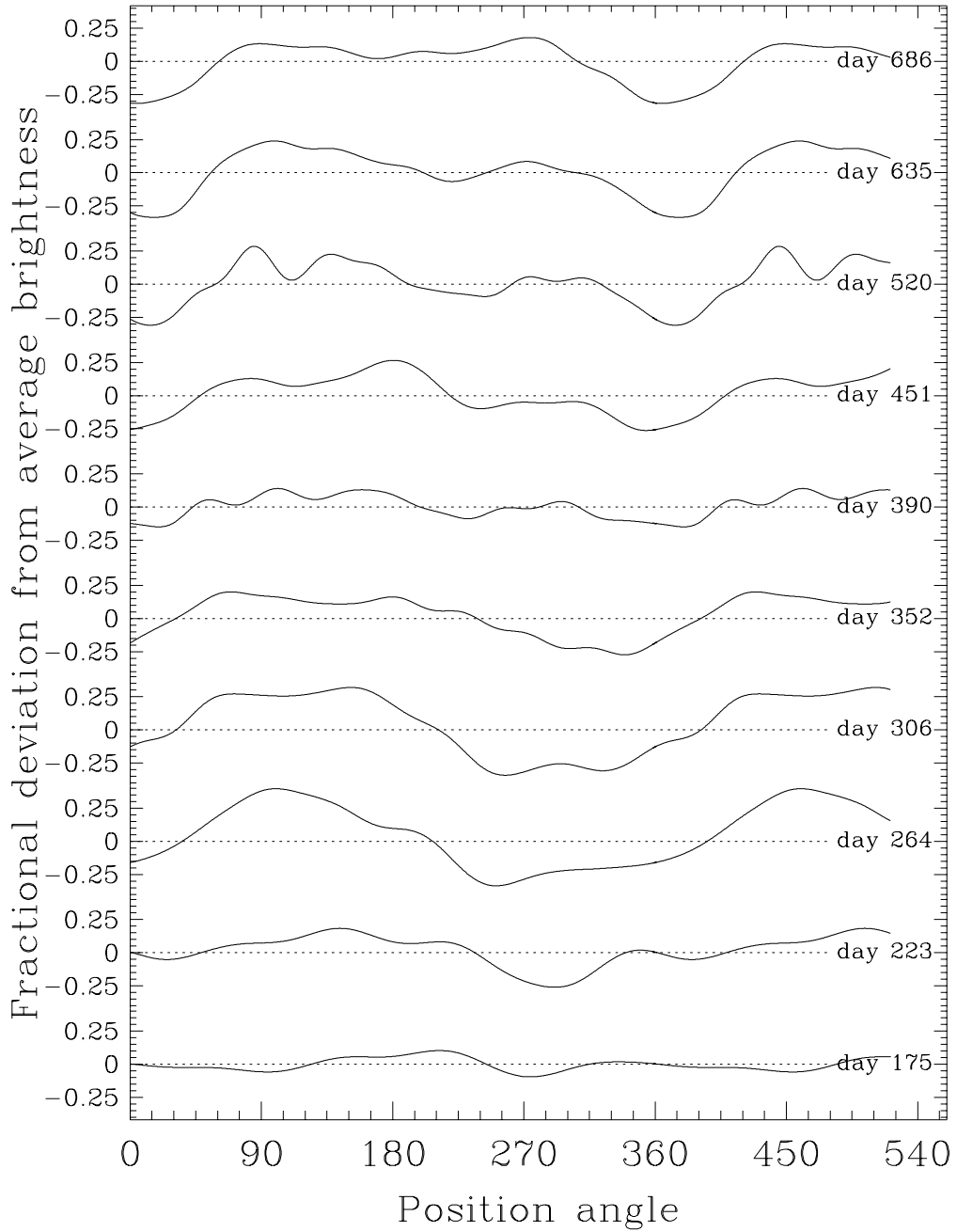


FIG. 9.— The variation of the brightness along the ridge as a function of position angle for several epochs of our observations, showing the coherent evolution at early epochs. Each of the curves shows the fractional deviation from the average brightness, integrated from 0.7 to $1.0\times$ the outer radius of the supernova as determined by model fits. The images used were those shown in Fig. 2. For a convenient display of the rotation of both the maximum and the minimum, we extend the position angle axis to 540° , causing some features to appear twice on each curve.

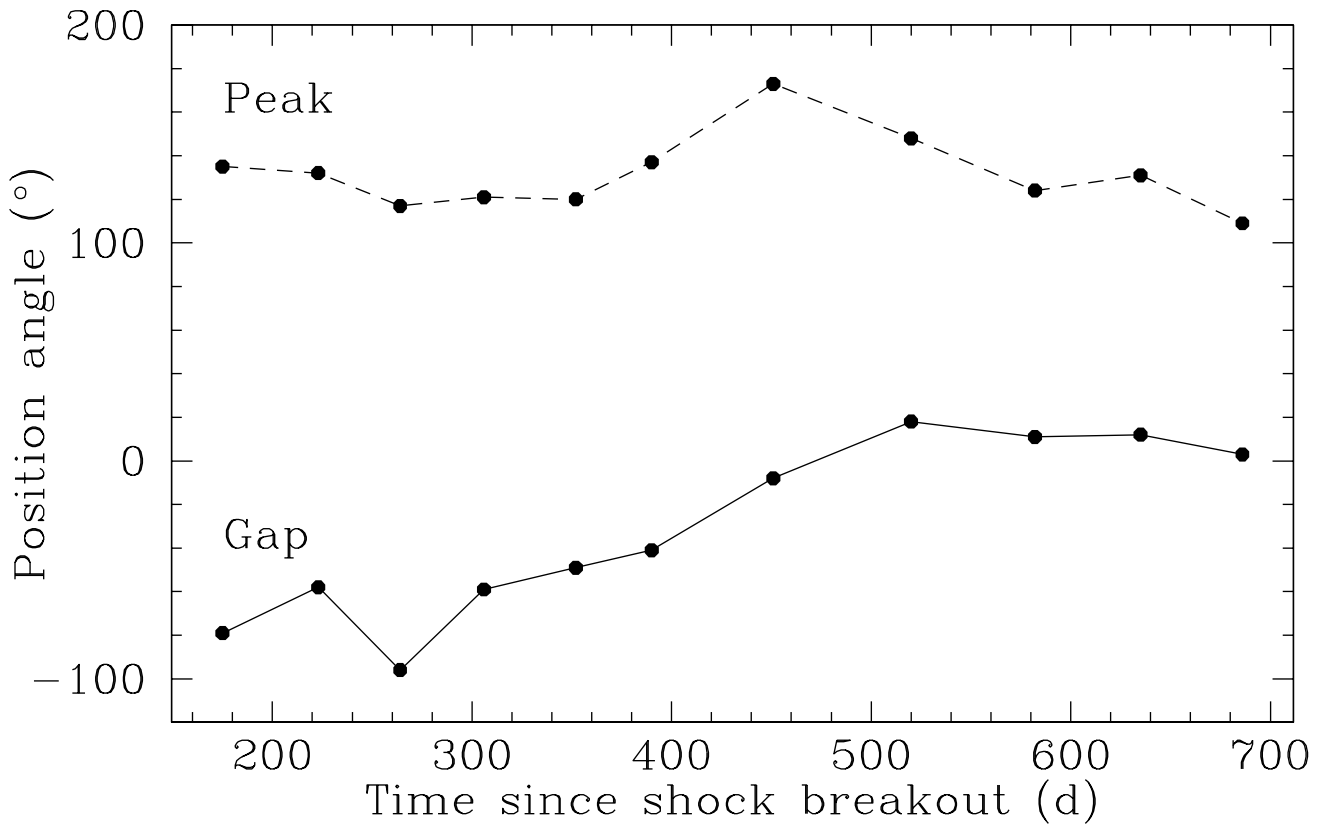


FIG. 10.— The position angle (p.a.) of the peak and gap in the brightness of the ridge as a function of time. The locations of the peak and the gap were determined from the images in Fig. 2, and the p.a.'s are referred to the geometric center of the radio shell. The p.a. of the gap was taken as that of the midpoint of the “horns” of the 64% contour, with the horns being the points on the contours with the largest curvature. The uncertainties are estimated to be $\sim \pm 10^\circ$.

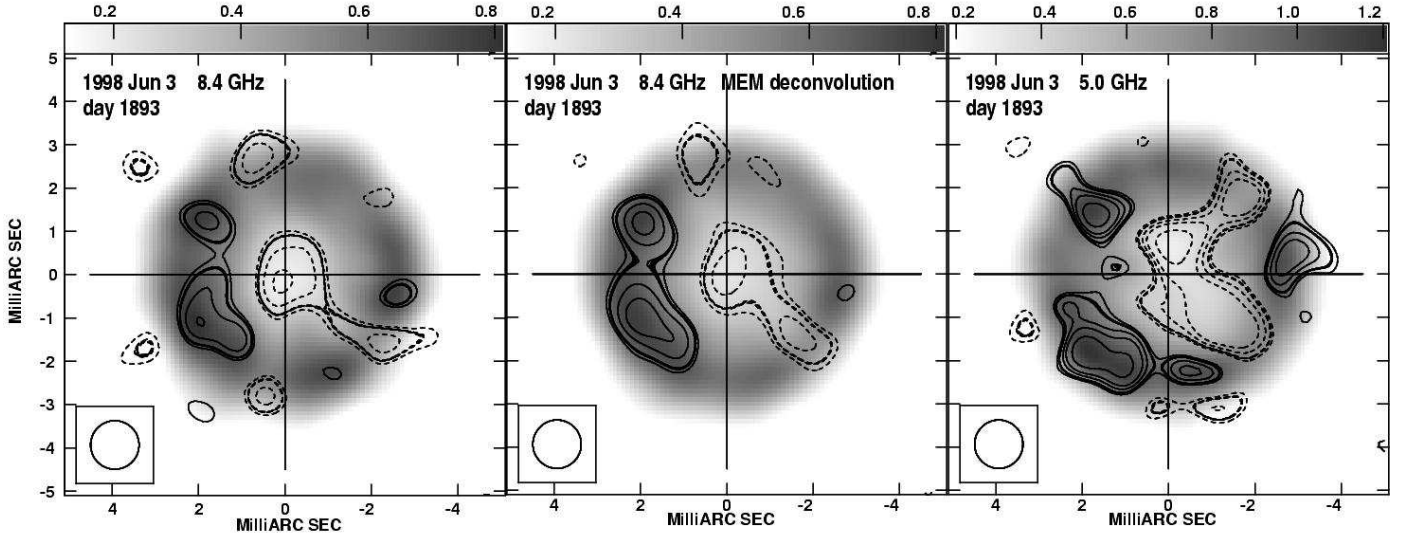


FIG. 11.— The deviation of the brightness distribution of the radio shell from the projection of a uniform spherical shell at $t = 1893$ d. The resolution is 1.12 mas. The greyscales, labeled in mJy beam^{-1} , represent the brightness in the deconvolved image. The contours represent, in units σ_{bg} , the deviations from the best-fit spherical shell model, also convolved to the same resolution. They are drawn at $-7, -5, -4, -3, -2.5, 2.5, 3, 4, 5$, and $7\sigma_{\text{bg}}$, with the $\pm 3\sigma_{\text{bg}}$ contours being emphasized. The true image uncertainty is $1.2\sigma_{\text{bg}} \sim 1.4\sigma_{\text{bg}}$ (see § 3.2). The contours thus indicate the significance of deviations from a uniform shell, with the extrema of both signs showing the most significant deviations. Features with amplitudes in excess of $\pm 3\sigma_{\text{bg}}$ are likely to be real, while features with lower amplitudes could be, but are not necessarily, due to image noise. The left panel shows the 8.4-GHz CLEAN image, the center panel shows an 8.4-GHz maximum entropy image, biased to be as near to the uniform shell as allowed by the data, and the right panel shows the 5.0-GHz CLEAN image.

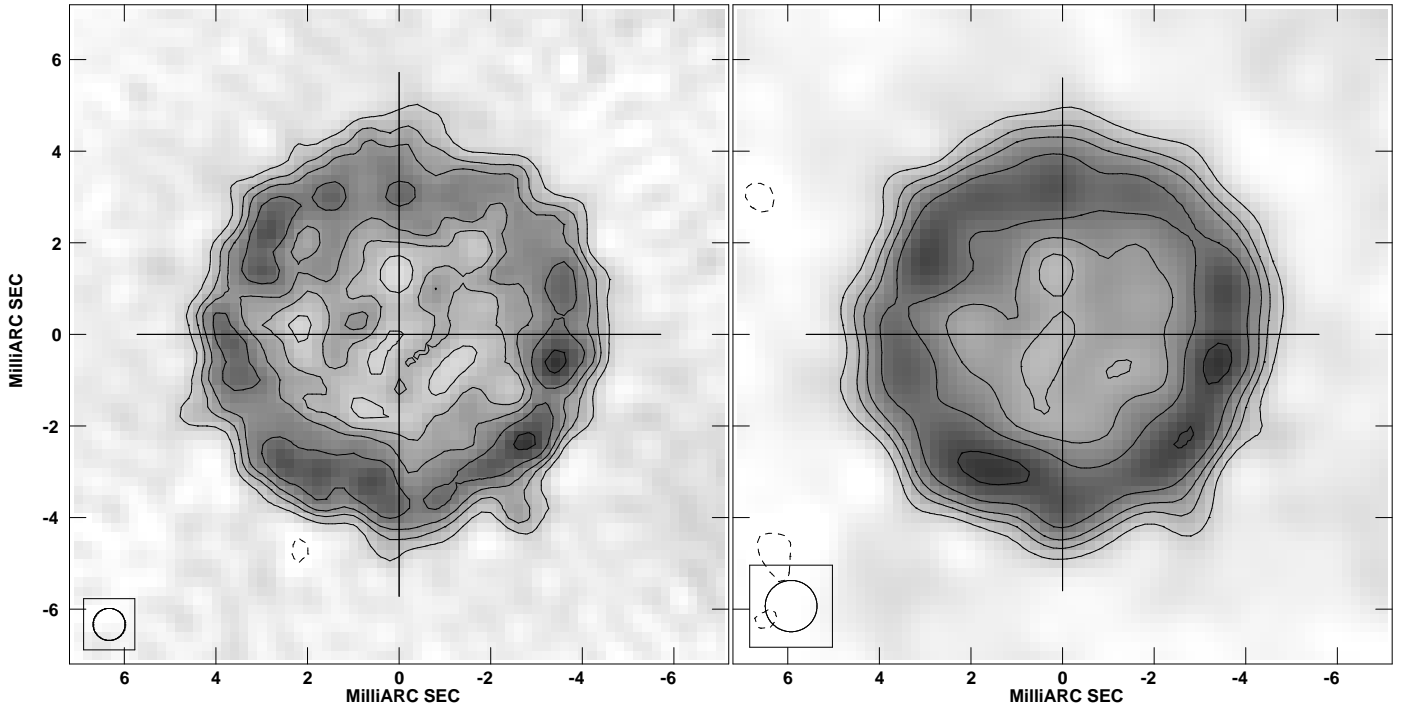


FIG. 12.— Composite images made from the 8.4-GHz data at $t = 2080$ d, 2525 d and 2787 d (1998 December, 2000 February and November), all aligned by the fit shell center, and scaled in flux density and radius to the values of the $t = 2787$ d data (i.e., $\theta_0 = 4.49$ mas; see text §4, 5 for details). The contours are drawn at $-16, 16, 32, 45.3, 64$ and 90% of the peak brightness, and σ_{bg} was 5% of the peak brightness on both images. On the left we plot an image with 0.70 mas resolution, and on the right one with the 1.12 mas resolution used for the individual epochs in Fig. 2.

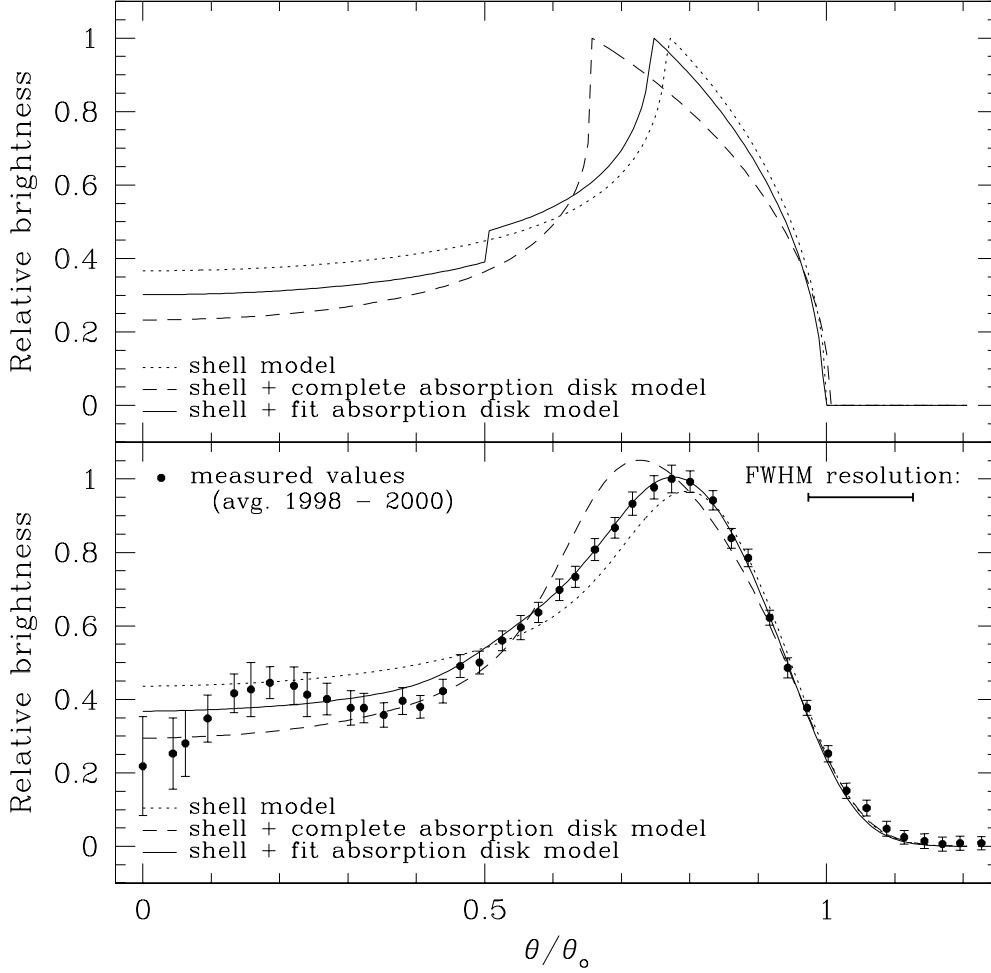


FIG. 13.— Radial profile of the relative brightness, averaged over all p.a.'s, versus angular radius, θ , for the period $2080 \text{ d} \leq t \leq 2787 \text{ d}$. We give θ in units of θ_o , the outer angular radius of the fit shell model. The radial profile is that of the composite image of Fig. 12. The profiles for several models are also plotted. The top panel shows the profile for three unconvolved models. The dotted line indicates the profile of the fitted spherical shell model, the dashed line that of the fitted model consisting of a uniform spherical shell with an absorption disk in the center which represents a completely opaque interior of the shell, and the solid line represents the best-fit model with a fitted absorption disk, representing incomplete absorption in the interior of the shell (§5). The lower panel shows the measured average profile and the profiles of the three models, all convolved to a resolution of $0.16 \theta_o$. The uncertainties indicated are the standard errors of the bin values, derived from the larger of the brightness uncertainty and the standard deviation within the bin and accounting for the number of beam areas within the bin. The plotted values are correlated, especially at small radii, because they are less than 1 beam width apart.

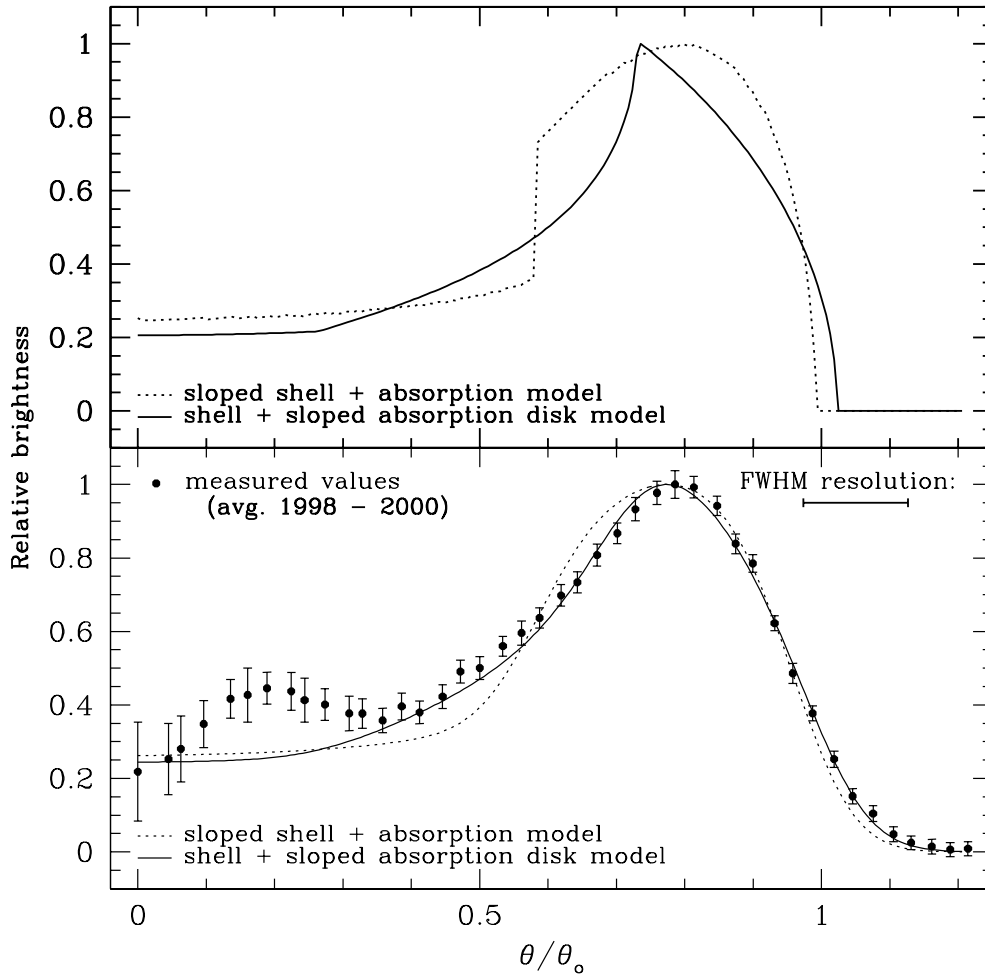


FIG. 14.— As Figure 13 above, but two alternate models are plotted. The dotted line shows a model which has complete absorption inside the inner radius of the shell, and volume emissivity that is zero at the inner radius of the shell and then rises linearly with radius till the outer radius of the shell. The inner radius was $0.56\times$ the outer radius. Such a model has the shallowest slope possible inside the ridge line. A good fit to the inside of the ridge line cannot be obtained with such a model. The solid line shows a model with and complete absorption in the center, but a gradual transition to zero absorption at the inner radius of the shell, but with uniform volume emissivity within the shell. Specifically, the fraction absorbed by the disk is 100% from the center up to a radius of $0.4\times$ the inner radius of the shell, and decreases linearly with radius to 0% at the inner radius. The inner radius was $0.71\times$ the outer radius. Note that this fit is non-unique, hence the values of the model parameters are consistent with but not demanded by the data.